nature neuroscience

Article

https://doi.org/10.1038/s41593-024-01609-3

Myeloid cell replacement is neuroprotective in chronic experimental autoimmune encephalomyelitis

Received: 12 January 2023

Accepted: 22 February 2024

Published online: 21 March 2024

Check for updates

Marius Marc-Daniel Mader[1,2], Alan Napole[1,2,5], Danwei Wu[1,2,3,5], Micaiah Atkins[4], Alexa Scavetti[1,2], Yohei Shibuya[1,2], Aulden Foltz[4], Oliver Hahn[4], Yongjin Yoo[1,2], Ron Danziger[1,2], Christina Tan[1,2], Tony Wyss-Coray[4], Lawrence Steinman[3] & Marius Wernig[1,2]

Multiple sclerosis (MS) is an autoimmune disease characterized by demyelination of the central nervous system (CNS). Autologous hematopoietic cell transplantation (HCT) shows promising benefits for relapsing–remitting MS in open-label clinical studies, but the cellular mechanisms underlying its therapeutic effects remain unclear. Using single-nucleus RNA sequencing, we identify a reactive myeloid cell state in chronic experimental autoimmune encephalitis (EAE) associated with neuroprotection and immune suppression. HCT in EAE mice results in an increase of the neuroprotective myeloid state, improvement of neurological deficits, reduced number of demyelinated lesions, decreased number of effector T cells and amelioration of reactive astrogliosis. Enhancing myeloid cell incorporation after a modified HCT further improved these neuroprotective effects. These data suggest that myeloid cell manipulation or replacement may be an effective therapeutic strategy for chronic inflammatory conditions of the CNS.

MS is the most common inflammatory neurological disorder in young adults[1]. Many patients will continue to accumulate neurological disabilities despite a number of available disease-modifying therapies, with a particular lack of treatment options for progressive MS[2–4]. There is growing evidence for the effectiveness of autologous hematopoietic cell transplantation (AHCT) in MS[5–9]. Although immunological changes in the peripheral blood have been reported[10–13], little is known about AHCT-induced changes within the CNS. Based on insights gained from animal models, most notably from EAE[14], it is acknowledged that cells of the CNS, including the astrocyte, oligodendrocyte and myeloid lineage, have relevant roles in the pathophysiology of neuroinflammation, exhibit broad reactive changes and can even be potential contributors to a disease-promoting or reparative environment[15–18]. Particularly, the role of microglia is complex, displaying the ability to promote both inflammation and remyelination[19–21]. Single-cell RNA sequencing technology has depicted vast transcriptional alterations in acute EAE; however, the late chronic stages are less well illuminated[22,23]. Notably, prior studies have demonstrated that busulfan-conditioned bone marrow transplantation (BMT) leads to CNS engraftment of donor-derived myeloid cells in murine models, raising the question of a potential role of microglia replacement in AHCT for MS[24,25].

In this study, we sought to investigate the CNS-specific mechanistic basis of AHCT-induced remission with the ultimate goal of assessing the cellular effects of syngeneic BMT. Using single-nucleus RNA

[1]Institute for Stem Cell Biology and Regenerative Medicine and Department of Pathology, Stanford University School of Medicine, Stanford, CA, USA. [2]Department of Pathology, Stanford University School of Medicine, Stanford, CA, USA. [3]Department of Neurology and Neurosciences, Division of Neuroimmunology and Multiple Sclerosis Center, Stanford University of Medicine, Stanford, CA, USA. [4]Department of Neurology and Neurological Sciences, Stanford University School of Medicine, Stanford, CA, USA. [5]These authors contributed equally: Alan Napole, Danwei Wu
e-mail: wernig@stanford.edu

sequencing (NucSeq), we provide a transcriptional characterization of the chronic phase of EAE in the context of BMT and augmented microglia replacement. We find that the CNS myeloid population is not only subjected to extensive quantitative and qualitative changes but also appears to functionally contribute to neuroprotective mechanisms.

Results

NucSeq reveals transcriptional activation in myeloid cells

To assess the unbiased transcriptional responses of different CNS cell types in chronic EAE with and without BMT, we conducted a NucSeq experiment on the thoracolumbar segment of spinal cords 3 months after myelin oligodendrocyte glycoprotein (MOG) peptide immunization (Fig. 1a and Extended Data Fig. 1a). In this chronic phase, we observed the persistence of demyelinating lesions with characteristic immune cell infiltrations of Iba1$^+$ myeloid cells (Fig. 1b). We enriched for nuclei with low expression of the neuronal marker NeuN for a higher representation of immune cells and glia (Fig. 1a and Extended Data Fig. 2a). Although there was no significant difference in the NeuN$^-$ percentage between samples, we observed an increase in the Olig2$^-$ fraction in EAE animals (Fig. 1c and Extended Data Fig. 2b). Nuclei derived from animals with similar clinical scores within one experimental group were pooled, and eight sequencing libraries were generated from 14 spinal cords (Extended Data Fig. 1a). After quality control, the integrated dataset consisted of 68,593 nuclei. Yield and quality metrics were comparable between the libraries (Extended Data Fig. 1b,c). Based on dimensionality reduction and unsupervised clustering, we identified several cell clusters (Extended Data Fig. 1d,e) corresponding to 12 distinct populations of main CNS cell types (Fig. 1d,e and Supplementary Table 1).

First, we sought to characterize the chronic EAE model by comparing control (healthy control without EAE induction) and EAE (EAE without intervention) groups. As expected, we observed a substantial change in cellular composition, with a prominent increase in myeloid cells and appearance of lymphocytes and a relative decrease in astrocytes and oligodendrocytes (Fig. 1f). In addition, chronic EAE also induced stark transcriptomic changes within different cell types of the spinal cord. Differential gene expression analysis between the control and EAE groups for each of the 12 cell clusters returned a total of 3,369 unique significantly differentially expressed genes (DEGs; adjusted P value (P_{adj}) < 0.05; Supplementary Table 2). Myeloid nuclei showed the highest number of DEGs (1,760), followed by oligodendrocyte lineage cells (1,470) and astrocytes (1,026; Fig. 1g and Extended Data Fig. 1f). Myeloid cells demonstrated a prominent enrichment for pathways associated with lipid metabolism, signaling and growth (Extended Data Fig. 3a,b and Supplementary Table 3). Astrocytes and oligodendrocytes showed a downregulation of energy-related pathways in combination with an upregulation of inflammatory pathways (Extended Data Figs. 3a,c and 4a,b). This was exemplified by an upregulation of *C4b*, and we histologically confirmed the increased expression of complement component 4 (C4; Extended Data Fig. 4c). Focusing on the main cell populations of the dataset, we used DEG-derived gene signatures specific for the myeloid, oligodendrocyte and astrocyte lineages (Fig. 1g and Supplementary Table 4) to calculate EAE scores, which showed cell type-specific expression changes between control and EAE groups (Fig. 1h)[26,27].

We confirmed the specificity of the above-described changes in an additional control cohort using the same nuclear sorting pipeline for subsequent NucSeq with cell hashing (Extended Data Fig. 5a–c). This included four additional healthy control animals with PBS injections and four animals with complete Freund's adjuvant (CFA) injections (without $MOG_{35–55}$). CFA animals developed prominent skin lesions at the injection sites and were analyzed 25 days post injection. We identified similar cell clusters as in the main dataset with the exception of T cells (no detectable expression of *Cd3e*; Extended Data Fig. 5d,e and Supplementary Table 5). The relative distribution of cell clusters was comparable to the control sample of the main cohort (Extended Data Fig. 5f,g). CFA led to comparatively small transcriptional changes compared to EAE (Extended Data Fig. 5h,i and Supplementary Table 6). Reassuringly, the expression of the above-established EAE cell type-specific scores was overall low in PBS and CFA groups of the control cohort and comparable to the control sample of the main cohort (Extended Data Fig. 5j).

Here, we provide a transcriptional characterization of the chronic stage of EAE, adding to the limited molecular knowledge of this translationally relevant phase of the disease model. We have generated a web application featuring a simplified, easily accessible version of our NucSeq dataset (https://werniglab.shinyapps.io/scthi/).

Myeloid expansion is a shared feature of chronic EAE and MS

To explore the translational relevance of our EAE gene expression data, we compared DEGs of the main cell populations with large-scale MS genome-wide association studies (GWAS) data[28]. Of 203 human MS susceptibility genes, we matched 197 mouse homologs, of which 43 (21.8%) were significantly differentially expressed in either the myeloid, oligodendrocyte and/or astrocyte lineage (Fig. 1i). Myeloid cells were the cell type with most matching DEGs, with *Iqgap1* representing the gene with the strongest myeloid specific expression change. *Nlrc5* was overexpressed in all main cell clusters, with the strongest effect in astrocytes. Correspondingly, we observed high expression of the protein NOD-like receptor family CARD domain containing 5 (NLRC5) in chronic EAE lesions as well as colocalization with GFAP$^+$ cells (Fig. 1j).

To further investigate similarities of the chronic EAE model with human MS pathobiology, we integrated and re-analyzed human NucSeq datasets derived from post-mortem spinal cord or brain tissue[29–32]. Although we observed differences in the total number of nuclei and features of the parent datasets (Extended Data Fig. 6a,b), clustering of the integrated datasets delineated major CNS populations that were mostly represented by all parent datasets, albeit in varying frequencies (Extended Data Figs. 6c–f and 7a and Supplementary Tables 7 and 8). Despite this heterogeneity, we observed an increase in myeloid and lymphoid cells in the brain, which was most prominent in active/chronic active (A/CA) lesions (Extended Data Fig. 7b). Remarkably, 55.2% (580 out of 1,050) and 55.1% (98 out of 178) of significant DEGs in the human brain and spinal cord MS datasets, respectively, were shared with chronic EAE DEGs (Supplementary Tables 9 and 10; based on 2,871 human orthologs identified out of 3,369 significant DEGs between control and EAE). Myeloid cells were again among the populations with the highest number of DEGs (Extended Data Fig. 7c). The human ortholog of the EAE myeloid score was increased in white matter and A/CA lesions in the brain (Extended Data Fig. 7d). Subclustering of the immune cells of the human NucSeq datasets demonstrated myeloid heterogeneity and MS-specific changes (Extended Data Fig. 7e–g and Supplementary Tables 11 and 12). In the brain, MS led to a reduction of the homeostatic myeloid cluster M.1, with an increase in clusters M.3, M.5 and M.6, particularly in A/CA lesions. Especially brain clusters M.3 and M.6 demonstrated expression of the human-orthologous EAE myeloid score, and the GWAS gene *IQGAP1* was expressed in M.3 in A/CA lesions (Extended Data Fig. 7h,i).

Collectively, we identify cell-type dependent expression changes of genes in chronic EAE with relevance in MS, as previously demonstrated by GWAS studies, and furthermore confirm an expansion and transcriptional activation of myeloid cells in progressive MS, particularly in chronic active lesions of the brain, thus suggesting translational relevance of the chronic EAE model regarding myeloid pathobiology.

BMT in EAE normalizes myeloid cell density

Given the prominent EAE-associated changes in both gene expression and cellular abundance of immune cells, we next explored whether BMT would impact the CNS myeloid cell compartment. Busulfan-conditioned BMT in EAE animals (EAE-BMT) led to robust donor chimerism in the

https://doi.org/10.1038/s41593-024-01609-3

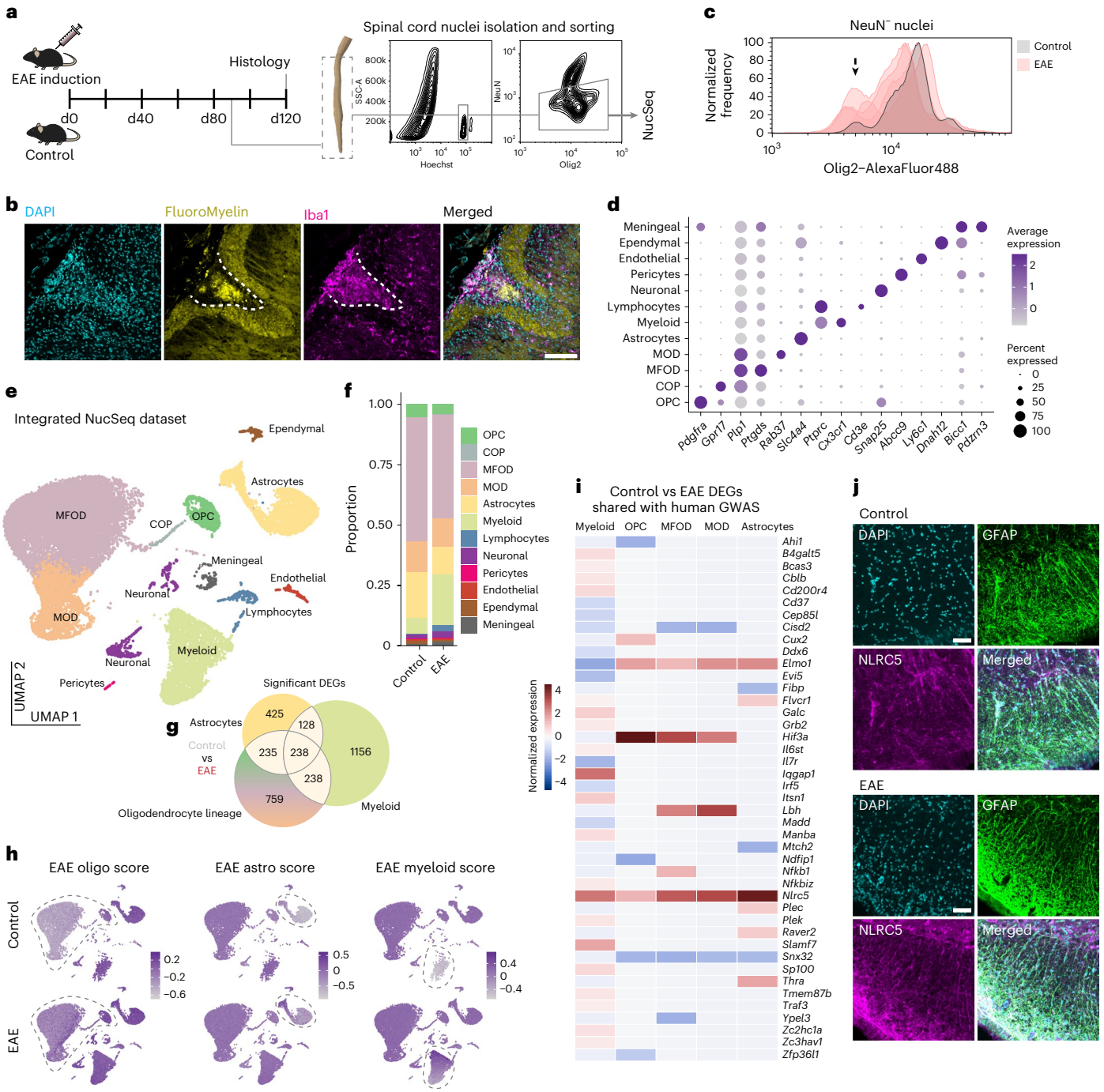


Fig. 1 | Myeloid expansion and transcriptional activation are features of chronic EAE. a, Experimental design and timeline. Representative image of the thoracolumbar section of the spinal cord used for NucSeq. Representative gating for flow-cytometric isolation of NeuN⁻ nuclei. **b**, Representative image of a lesion in the dorsal column of an EAE animal featuring immune infiltration and demyelination. Scale bar, 100 µm. **c**, Expression of Olig2 in NeuN⁻ nuclei of EAE and control animals measured by flow cytometry. Arrow indicates an increase in Olig2⁻ nuclei in the EAE condition (four EAE animals are shown). **d**, Annotation and canonical marker genes of main clusters. COP, committed oligodendrocyte precursor; MFOD, myelin-forming oligodendrocytes; MOD, mature oligodendrocytes; OPC, oligodendrocyte precursor cells. **e**, UMAP of 25,165 nuclei integrated from EAE and control libraries with annotation of main cell clusters. **f**, Distribution of cell populations between control and EAE animals. **g**, Venn diagram of DEGs of myeloid, astrocyte and oligodendrocyte lineage between control and EAE conditions with $P_{adj} < 0.05$ (MAST with Bonferroni correction). **h**, Disease scores were calculated with the VISION[26] pipeline using gene signatures based on cell type-specific DEGs. Score expression changes are shown between control and EAE groups. **i**, A total of 43 significant DEGs shared with genes of an MS GWAS[28] are demonstrated with their expression profiles over different cell populations. Expression values (average $\log_2$(fold change)) are normalized by columns. If no significant DEG was present for a cell type, the value 0 was applied. **j**, Representative images of control and EAE spinal cord tissue. The EAE tissue features a white matter lesion with astrogliosis and increased expression of NLRC5. Stain was evaluated in three independent EAE and three independent control spinal cords. Scale bar, 50 µm.

https://doi.org/10.1038/s41593-024-01609-3

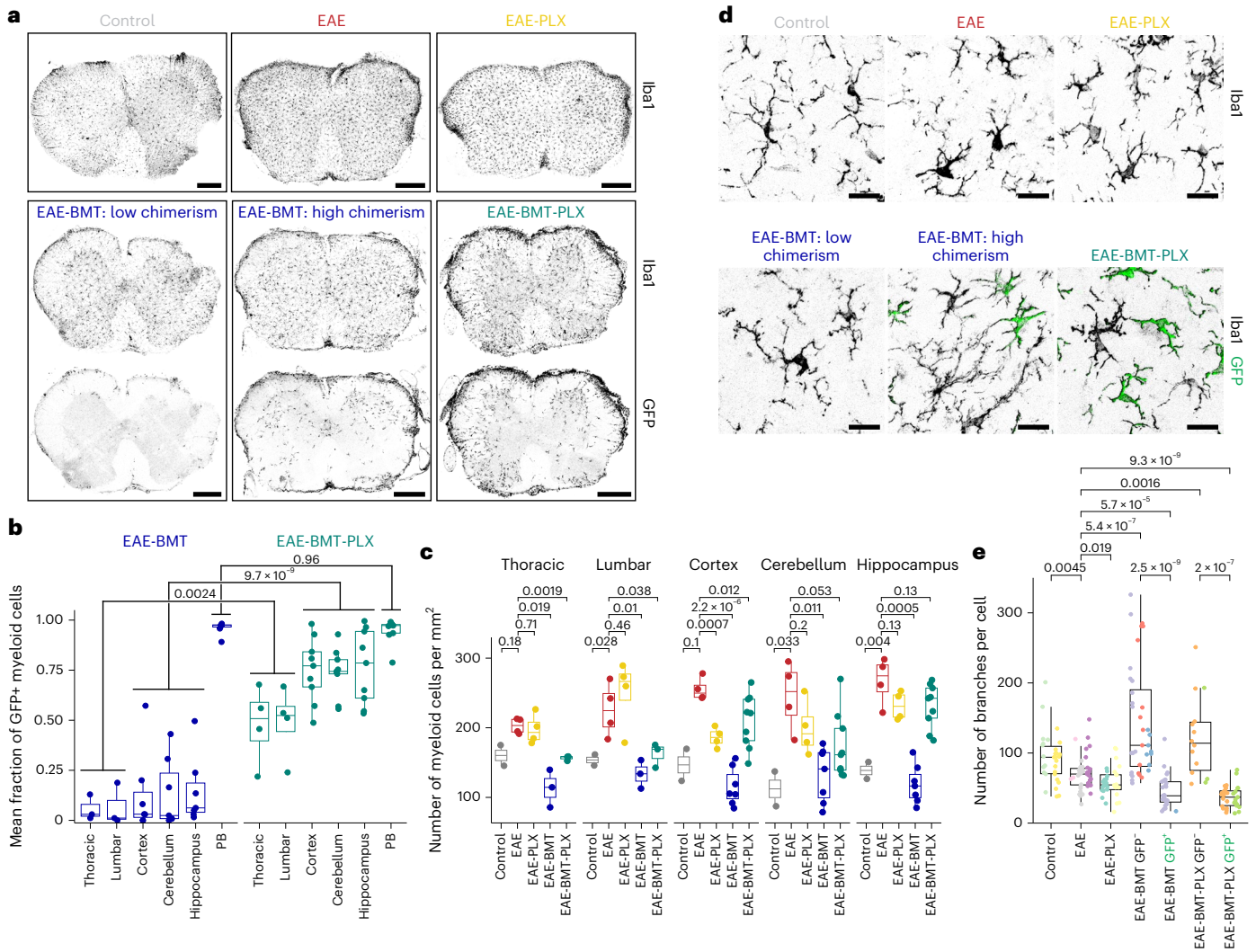


Fig. 2 | BMT changes the density and morphology of CNS myeloid cells in chronic EAE. a, Images of lumbar spinal cord sections demonstrating Iba1$^+$ myeloid cell distribution as well as engraftment of donor-derived GFP$^+$ cells (representative for a total of 17 spinal cords). Brightness, contrast and size were adjusted individually per image for illustrative reasons. Scale bars, 300 µm. **b**, Chimerism of donor-derived GFP$^+$ cells within the myeloid cell compartment (CNS tissue based on Iba1$^+$ immunofluorescence staining; peripheral blood (PB) based on CD45$^+$CD11b$^+$ gate in flow cytometry) for different tissues and compared between the EAE-BMT and EAE-BMT-PLX conditions. Replicates for brain and PB: $n = 7$ and $n = 9$ for EAE-BMT and EAE-BMT-PLX, respectively. Mean values are based on a total number of 136 brain regions of interest (ROIs). Spinal cords represent only animals not used for NucSeq; number of replicates: $n = 3$ and $n = 4$ for EAE-BMT and EAE-BMT-PLX, respectively, with mean values based on a total of 35 sections. Two-sided Mann–Whitney *U*-test. **c**, Quantification of ramified Iba1$^+$ cell density. Dots represent the average of multiple measurements per animal. A total number of 78 spinal cord ROIs and 221 brain ROIs were assessed derived from a total of 26 animals. Two-sided Welch *t*-test. **d**, Representative immunofluorescent images of ramified myeloid cells in the spinal cord. Brightness and contrast were adjusted individually per image for morphological assessment owing to differing Iba1 intensity between conditions. Scale bar, 20 µm. **e**, Quantification of branches of ramified myeloid cells of the spinal cord in different conditions. Each dot represents one cell (total $n = 210$); dot colors represent different animals ($n = 12$). Two-sided Mann–Whitney *U*-test. Boxplot elements represent the median (center line), first and third quartiles (lower and upper hinges) and smallest and highest values, at most 1.5× the inter-quartile range from the hinge (whiskers).

peripheral blood and myeloid infiltrates at demyelinated lesions but only low-level engraftment of transplanted circulation-derived myeloid cells (CDMCs) in both brain and spinal cord (Fig. 2a,b and Extended Data Fig. 8a,b). We and others previously reported that transient colony-stimulating factor 1 receptor (CSF1R) inhibition after BMT can substantially increase the incorporation of such CDMCs into the brain of healthy mice[24,25,33–35]. To functionally interrogate the role of CDMCs in chronic EAE, we subjected EAE animals to 10-day CSF1R inhibition with PLX5622 after BMT (EAE-BMT-PLX; Extended Data Fig. 1a). This led to a significant increase in engraftment efficiency of CDMCs in the CNS with higher chimerism in the brain compared to the spinal cord (Fig. 2a,b and Extended Data Fig. 8b–d). Accordingly, expression of a CDMC score based on previous transcriptional data exhibited a strong increase in EAE-BMT-PLX (Extended Data Fig. 8e,f and Supplementary Table 4)[25].

Astonishingly, the EAE-induced increase in myeloid density in the spinal cord was normalized in both BMT groups but not in a PLX5622-only control group without BMT (EAE-PLX; Fig. 2c). Furthermore, we observed a change in myeloid cell morphology in association with both disease and intervention (Fig. 2d,e and Extended Data Fig. 8g–i). As expected, Iba1$^+$ myeloid cells were less ramified in chronic EAE than in healthy control mice. Engrafted GFP$^+$ CDMCs were even less ramified, in line with previous findings[25,33,35]. However, remaining endogenous CNS-resident GFP$^-$ microglia showed a pronounced increase in complexity in both BMT conditions, exceeding the ramification in healthy mice.

Together, these findings demonstrate that BMT globally impacts CNS myeloid cells not only by the integration of donor-derived myeloid cells but also by altering the distribution and morphology of endogenous microglia.

BMT promotes EAE remission and a reactive myeloid state

The EAE model led to initial peak clinical severity ~15 days post induction, with a similar clinical score between all experimental groups before any interventions (Fig. 3a,b). Animals of the EAE group continued to exhibit severe neurological symptoms over the chronic course, with almost all animals presenting with complete hind leg paralysis at 3 months. We observed clinical improvement starting in close temporal relationship to BMT on day 25, resulting in a significantly reduced clinical score on day 40. The median clinical score of the EAE-BMT group remained reduced in the later phase but with increasing interindividual variability. The high-efficiency microglia replacement (EAE-BMT-PLX) led to a more robust clinical improvement; that is, preventing mortality and clinical scores of >3, and resulting in a continued significantly reduced overall clinical score. We did not detect sustained clinical benefits in the EAE-PLX group.

In line with the histological assessment (Fig. 2c), we observed a reduction of the EAE-associated increase in the nuclear fraction of myeloid cells with BMT (Fig. 3c). Similarly, the EAE-induced increase in lymphocyte nuclei was reduced following BMT. The interventions led to differentially changed gene expression within different cell subpopulations, with the myeloid cluster demonstrating the highest number of DEGs (Fig. 3d). We observed reduced expression of the EAE scores for astrocytes and oligodendrocytes in BMT conditions that correlated with the degree of paralysis (Fig. 3e,f). Surprisingly, the EAE myeloid score behaved in the opposite way, showing a further increase in both treatment groups.

Collectively, clinical improvement associated with BMT was accompanied by an overall reduced expression of EAE-specific gene signatures in oligodendrocytes and astrocytes in contrast to an increased expression in the myeloid lineage. These changes were further enhanced after augmented integration of CDMCs in EAE-BMT-PLX, suggesting a certain protective role of the myeloid response in chronic EAE that can be further enhanced by manipulation of the myeloid compartment.

BMT reduces demyelination and reactive astrogliosis

Next, we aimed to further characterize BMT-induced changes in the oligodendrocyte and astrocyte lineages. The majority of DEGs between EAE and EAE-BMT were also shared between EAE and EAE-BMT-PLX, while the latter condition featured a relevant number of additional DEGs (Extended Data Fig. 9a). We observed a negative correlation of EAE-specific DEGs (EAE vs control) with intervention-specific DEGs (EAE vs EAE-BMT or EAE-BMT-PLX), in line with the directionality of EAE scores. This suggests that EAE-induced transcriptional changes are partially reversed by BMT and microglia replacement (Extended Data Fig. 9b). Pathway enrichment analysis revealed the upregulation of neuroprotective pathways in oligodendrocytes and astrocytes such as neurogenesis for EAE-BMT-PLX, whereas these signals were less prominent in EAE-BMT (Fig. 4a and Extended Data Fig. 9c). Such transcriptomic changes were further corroborated by histopathological alterations: demyelination remained a common histopathological feature in chronic EAE (Fig. 4b). The area of demyelination correlated with clinical severity, which was most significant for the cervical and lumbar segments (Extended Data Fig. 9d). Importantly, BMT led to a significant reduction in demyelinated areas in the cervical and lumbar spinal cord, which was further enhanced in the EAE-BMT-PLX group for the cervical segment (Fig. 4b,c). Correspondingly, we observed the upregulation of several key myelination and oligodendrocyte differentiation genes (Fig. 4d). *Daam2*, which has been reported to inhibit oligodendrocyte differentiation, was reduced in its expression[36].

Deeper characterization of astrocytes revealed two major groups of subclusters with either high expression of marker genes such as *Gpc5* and *Trpm3* (subclusters Astro.1 to Astro.5) or *Glis3*, *Aqp4*, *A2m* and *Gfap* (subclusters Astro.6 and Astro.7; Fig. 4e, Extended Data Fig. 9e and Supplementary Table 13). Subclusters Astro.6 and Astro.7 also expressed *Serping1* and *Ggta1* (ref. 37), the GWAS gene *Nlrc5* and the EAE astro score (Fig. 4f). Fittingly, the most prominent changes in subcluster distribution between different conditions concerned subclusters Astro.6 and Astro.7, which were increased in EAE and subsequently reduced in the BMT groups (Fig. 4g). Moreover, we observed expression changes of pro-inflammatory genes within different subclusters (particularly prominent for Astro.5), with an increase in EAE that was ameliorated in BMT conditions (Fig. 4h and Extended Data Fig. 9f). We confirmed these transcriptional findings by histological quantification of GFAP immunoreactive areas[38], which were increased in the EAE condition and reduced in BMT conditions (Fig. 4i,j).

Together, we find that functional recovery of EAE animals treated with BMT regimens is accompanied by improved myelination patterns, enrichment in neuroprotective gene expression and reduced reactive astrogliosis. Notably, such changes were of a stronger extent when BMT was accompanied by subsequent CSF1R inhibition.

BMT modulates the heterogeneity of CNS immune cells in EAE

Given the apparent prominent role of myeloid cells in the pathobiology of chronic EAE, we next performed a subcluster analysis of the immune cluster, which delineated nine myeloid as well as a T cell and natural killer cell (TC+NK) and a small B cell subcluster (Fig. 5a,b and Supplementary Table 14).

BMT interventions not only led to an overall reduced number in lymphocyte nuclei (Fig. 3c), but we also observed a shift in lymphocyte distribution within the TC+NK subcluster (Fig. 5c,d, Extended Data Fig. 10a and Supplementary Table 15). Although chronic EAE led to an elevated fraction of *Rora*$^+$ effector T cells, this fraction was reduced in the treatment groups. The TC+NK subcluster distribution shifted more towards a composition as seen in the control condition, except for a persistently elevated fraction of *Foxp3*$^+$*Ctla4*$^+$ regulatory T cells. This suggests that BMT drives the CNS T cell compartment away from a pro-inflammatory towards a more immunosuppressive state. This is particularly interesting given a recent report that microglia directly influence the CNS T cell composition in a relapsing–remitting EAE model, particularly affecting the balance of effector and regulatory T cells[39].

Although BMT led to a reduction in overall spinal cord myeloid cells (Figs. 2c and 3c), we observed an increase in heterogeneity (Fig. 5e). We found that myeloid subclusters could be stratified into three groups with either the expression of canonical homeostatic microglia genes like *Tmem119*, *Cx3cr1* and *P2ry12* (M.1 to M.3), macrophage-specific and CDMC-specific genes like *Ms4a7* and *Lyz2* (M.7 to M.9) or a combination of both (M.4 to M.6) (Fig. 5a)[25,40,41]. Notably, although the EAE myeloid score reflected this grouping, with the highest expression in M.7 to M.9, the CDMC score expression showed a slightly different pattern, with the highest expression in M.6 and M.9 (Fig. 5f). Moreover, the EAE-BMT-PLX condition induced an increase in CDMC score expression within subclusters, particularly for cluster M.8. In line with these findings, nuclei in which expression of GFP was detected—which was only a small number in our dataset, suggesting overall low expression levels of the transgene—localized mostly with subclusters M.9 and M.6 in EAE-BMT and more broadly, including M.8, in EAE-BMT-PLX (Extended Data Fig. 10b). We sought to further confirm this association by exploring the expression of CD206 (encoded by *Mrc1*), which is a CDMC score but not EAE myeloid score gene and highly expressed in cluster M.6. Based on immunofluorescence analysis, we confirmed overall higher but variable protein levels of CD206 in GFP$^+$ graft-derived cells (Fig. 5g,h). CD206 is also known as a marker for border-associated macrophages, which we observed in all conditions.

https://doi.org/10.1038/s41593-024-01609-3

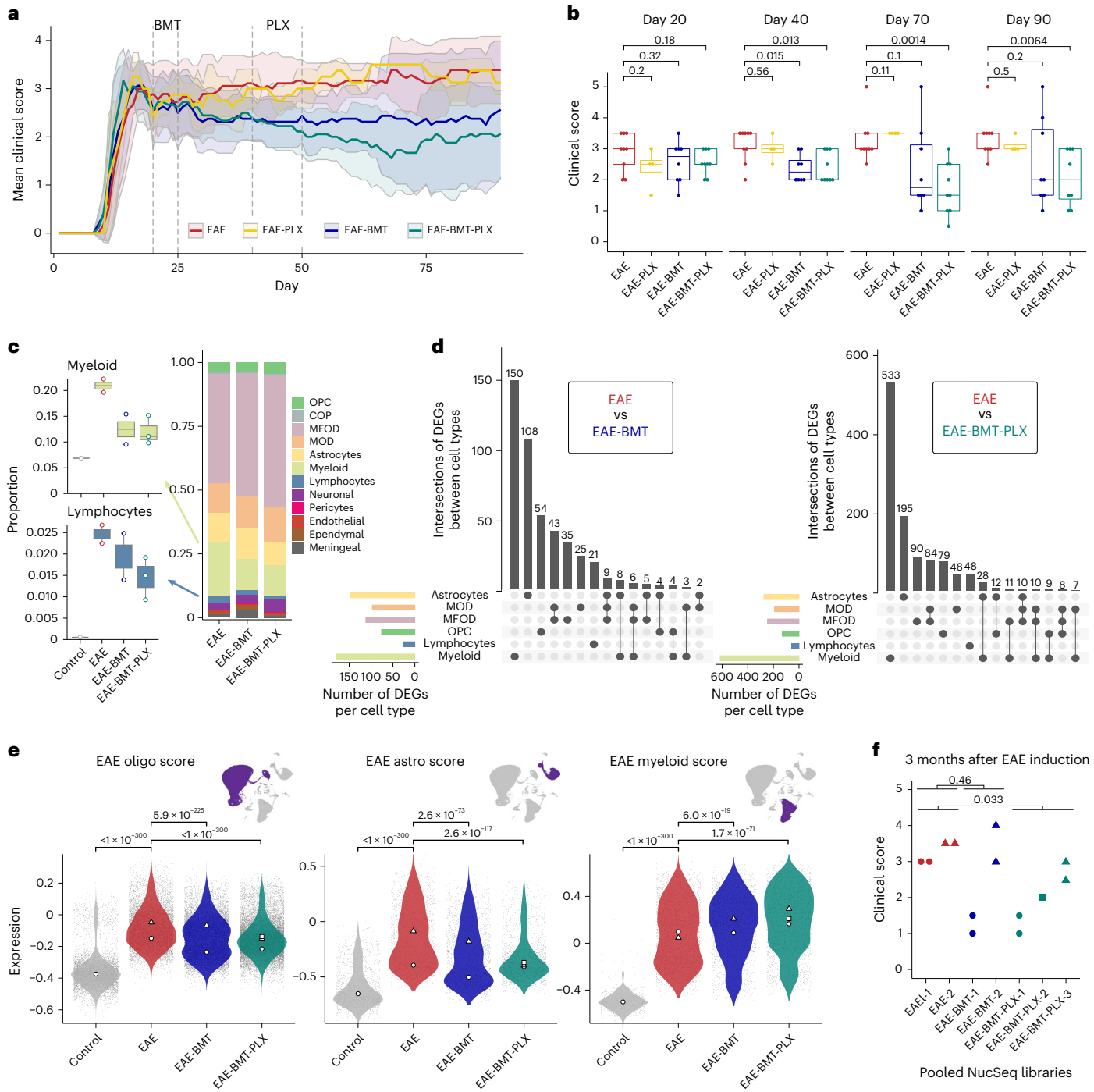


Fig. 3 | BMT and microglia replacement enhance the myeloid transcriptional response and improve clinical outcome. a, Mean clinical score ± standard deviation over an observation period of 90 days. In total, 30 animals derived from two independent cohorts were included (EAE, $n = 9$; EAE-BMT, $n = 8$; EAE-BMT-PLX, $n = 9$; EAE-PLX, $n = 4$). Two animals showed EAE-related mortality before completion of the observation period (EAE, day 68; EAE-BMT, day 66). One animal of the EAE-BMT-PLX group was killed on day 76 for reasons unrelated to EAE (with a clinical score of 1.5) and was excluded from the analysis after that timepoint. **b**, Distribution of clinical scores for the indicated timepoints (based on $n = 30$ animals total). Two-sided Mann–Whitney *U*-test. **c**, Fractions of nuclei of main cell types in different conditions (based on total $n = 8$ sequencing libraries derived from 14 spinal cords). **d**, Significant DEGs ($P_{adj} < 0.05$) for main cell types between the EAE and EAE-BMT or EAE-BMT-PLX groups. The top 15 intersections are illustrated. **e**, Expression changes of EAE scores for main cell types. White markers show the median of individual NucSeq libraries. P_{adj} values based on two-sided Mann–Whitney *U*-test with Holm method adjustment. **f**, Clinical score of EAE animals pooled for different NucSeq libraries at the timepoint of tissue collection. Marker shape corresponds to panel e. Two-sided Mann–Whitney *U*-test. Boxplot elements represent the median (center line), first and third quartiles (lower and upper hinges) and smallest and highest values, at most 1.5× the inter-quartile range from the hinge (whiskers).

In the control condition, about 75% of all myeloid cells localized to clusters M.2 and M.5 (Fig. 5e), both of which were reduced in EAE conditions and additionally showed a reduction in homeostatic microglia gene expression, most dramatically in M.5 (Extended Data Fig. 10c and Supplementary Table 16). Thus, chronic EAE was associated with a shift in CNS myeloid cells away from a homeostatic state toward

https://doi.org/10.1038/s41593-024-01609-3

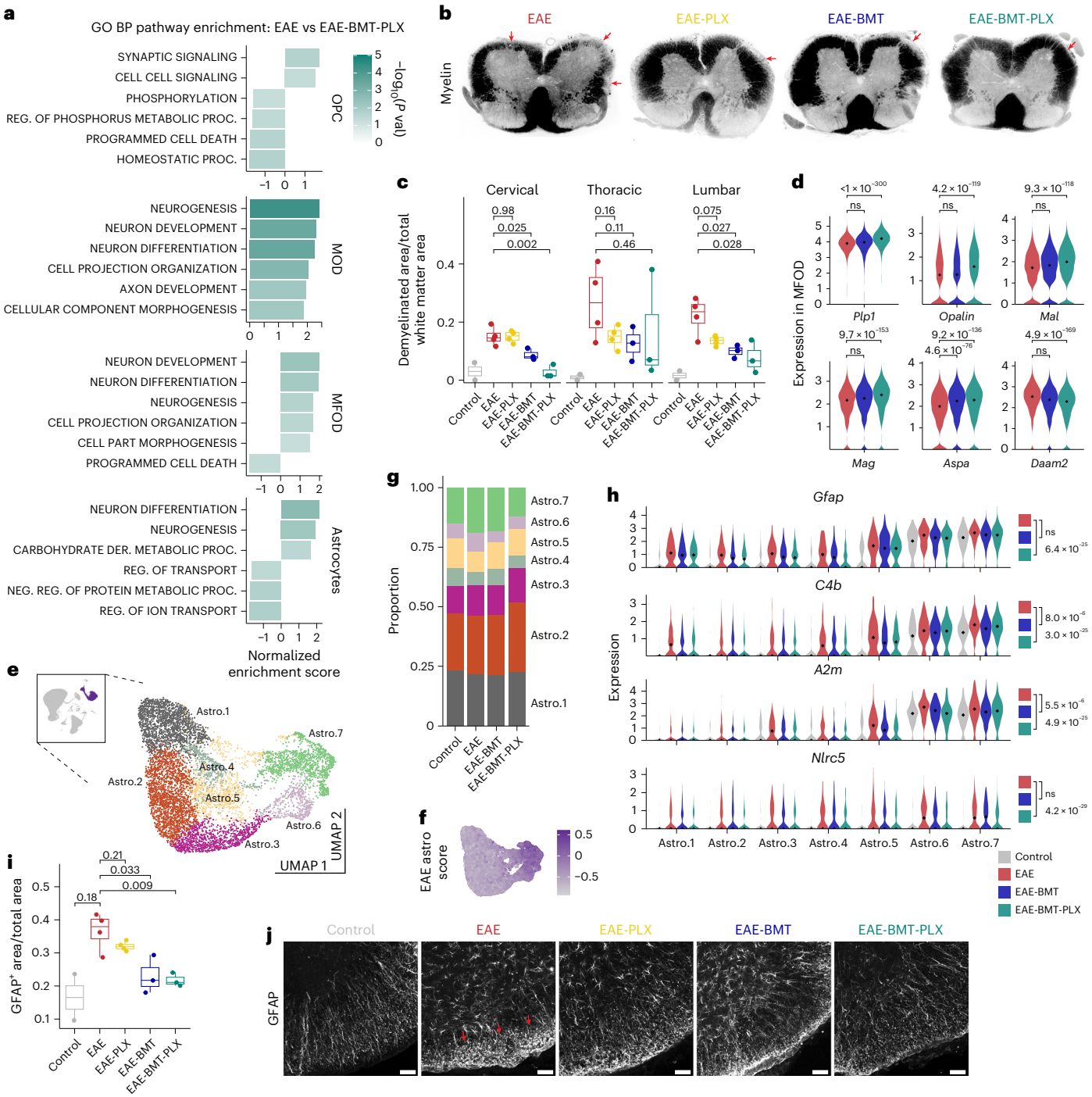


Fig. 4 | BMT reduces spinal cord demyelination and reactive astrogliosis. **a**, Gene set enrichment analysis (GSEA) based on DEGs between the EAE and EAE-BMT-PLX groups in selected clusters. Positive values indicate pathway enrichment in upregulated genes; negative values indicate enrichment in downregulated genes. Shown are the top six Gene Ontology (GO) biological process (BP) pathways based on GSEA-derived *P* values[56]. Terms are abbreviated to fit the format. A complete list can be found in Supplementary Table 3. **b**, Representative fluorescent myelin stain (FluoroMyelin) of the lumbar spinal cord. Red arrows indicate demyelinated lesions. **c**, Comparison of demyelinated white matter areas between conditions for animals with available spinal cord histology. Dots represent the average of multiple analyzed spinal cord sections, with a median of four (range of two to six) sections per anatomical location per animal ($n = 16$ animals total). Two-sided Welch *t*-test. **d**, Violin plots of selected genes associated with myelin formation and oligodendrocyte differentiation that are differentially expressed between EAE and treatment conditions. P_{adj} values are displayed (DEG analysis based on the MAST algorithm; see also Supplementary Table 2). Genes indicated as 'ns' were not returned by the DEG analysis. Diamond markers indicate the median. **e**, UMAP plot of the astrocyte cluster with subclusters consisting of a total of 7,745 nuclei. **f**, Expression of the EAE astro score. **g**, Distribution of astrocyte subclusters between different conditions. **h**, Expression of selected genes associated with reactive astrogliosis. P_{adj} values based on DEG analysis between different conditions for the whole astrocyte cluster (MAST algorithm; see also Supplementary Table 2). Genes indicated as 'ns' were not returned by the DEG analysis. Diamond markers indicate the median. **i**, Quantification of GFAP⁺ area in the lumbar spinal cord. Dots represent the average of measurements per animal (median = 2 spinal cord sections per animal). Two-sided Welch *t*-test. **j**, Representative images with immunofluorescent stain for GFAP in the lumbar spinal cord (a total of 16 spinal cords were evaluated). Scale bar, 50 µm. Red arrows indicate subdural astrogliosis in an EAE animal. Boxplot elements represent the median (center line), first and third quartiles (lower and upper hinges) and smallest and highest values, at most 1.5× the inter-quartile range from the hinge (whiskers).

https://doi.org/10.1038/s41593-024-01609-3

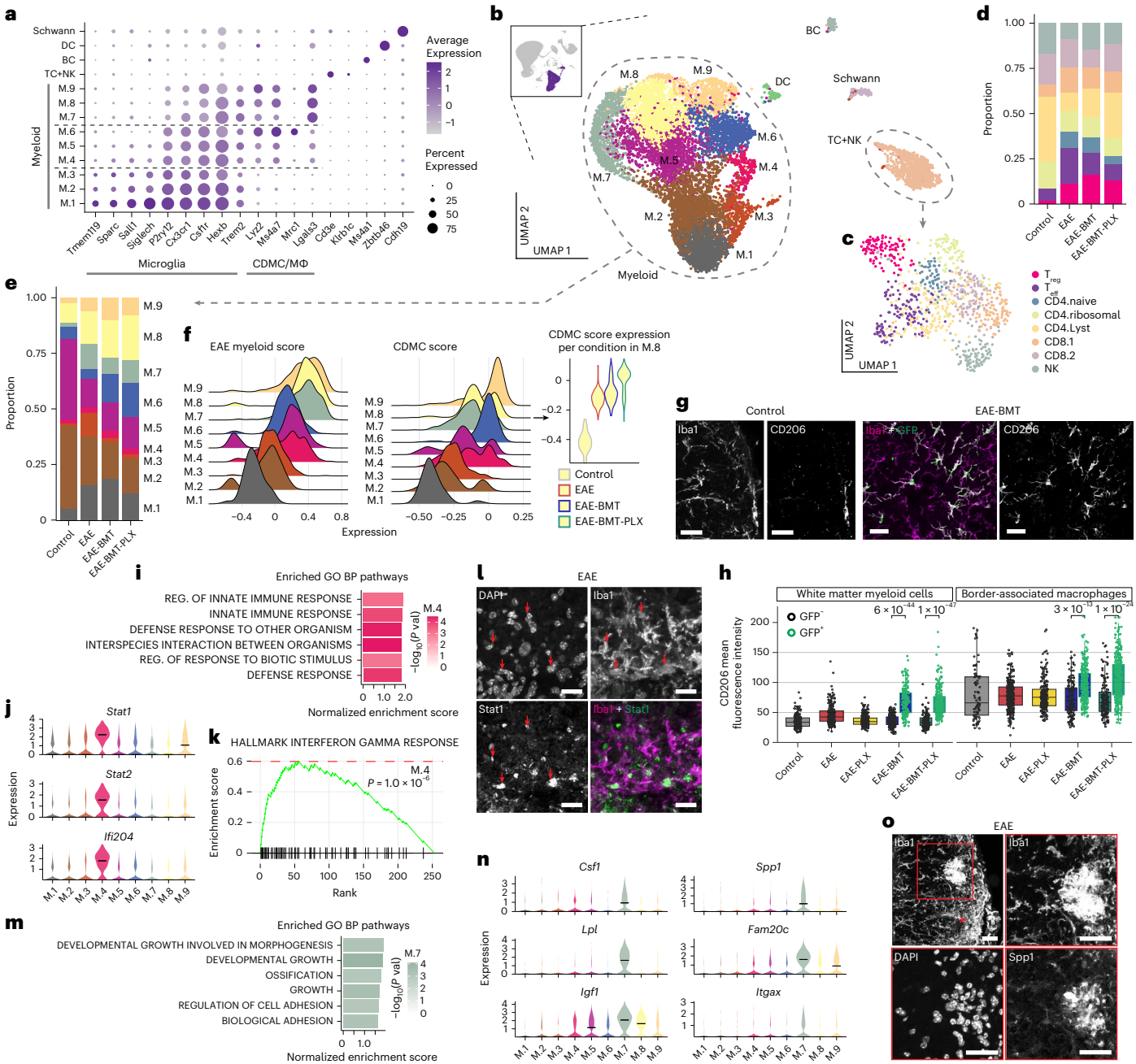


Fig. 5 | BMT modulates the heterogeneity of CNS immune cells in chronic EAE with persistence of DAM. a, Expression of marker genes in immune cell subclusters. BC, B cells; DC, dendritic cells; M, myeloid; MΦ, macrophages; NK, natural killer cells; TC, T cells. **b**, UMAP plot with 10,314 nuclei of the immune cluster. Subcluster analysis was performed on the immune cell clusters of the integrated main dataset (compare purple cluster in small insert, top left). **c**, UMAP plot of subclustered T cells representing 860 nuclei. T_{eff}, effector T cells; T_{reg}, regulatory T cells. **d**, Distribution of T cell subclusters between different conditions. **e**, Distribution of myeloid cell subclusters between different conditions. **f**, Expression of the EAE myeloid score and CDMC score in different myeloid subclusters. **g**, Immunofluorescent stain for CD206 (*Mrc1*) in the spinal cord of a control animal (left) and EAE-BMT animal (right). For replication, see panel h. Scale bars, 30 µm. **h**, Mean fluorescence intensity of CD206 in Iba1$^+$ cells in the spinal cord of 16 animals. Each dot represents a single cell. Two-sided Mann–Whitney *U*-test. **i**,**m**, GSEA for marker genes of the myeloid subcluster M.4 and M.7. The top GO BP pathways based on GSEA-derived *P* values are shown[56]. Abbreviations were used for illustrative reasons; the complete list can be found in Supplementary Table 17. **j**, Expression of M.4 marker genes in myeloid subclusters. **k**, GSEA enrichment plot for the Hallmark Interferon Gamma Response pathway in subcluster M.4 with GSEA-derived *P* value[56]. **l**, Immunofluorescent stain for Stat1 in a spinal cord white matter lesion of an EAE animal. Red arrows indicate nuclear and paranuclear Stat1 signal colocalizing with Iba1. Stain was evaluated in three independent EAE spinal cords. Scale bar, 20 µm. **n**, Expression of M.7 marker genes in myeloid subclusters. **o**, Immunofluorescent image of Osteopontin (Spp1)-positive myeloid cells with strong Iba1 signal forming a cluster adjacent to an inflammatory lesion (red asterisk) in the spinal cord of an EAE animal. Red square in top left panel indicates magnified area shown in other panels. Stain was evaluated in three independent EAE spinal cords. Scale bar, 30 µm. Boxplot elements represent the median (center line), first and third quartiles (lower and upper hinges) and smallest and highest values, at most 1.5× the inter-quartile range from the hinge (whiskers).

macrophage-associated gene expression profiles. This was further enhanced in the EAE-BMT and EAE-BMT-PLX groups owing to a relative increase in clusters M.8, M.9 and, most prominently, M.6 (Fig. 5e).

By contrast, M.4 and M.7 represented quantitatively stable clusters between EAE and treatment conditions. The small cluster M.4 demonstrated upregulation of immune and interferon gamma response pathways as well as overexpression of several previously reported injury-responsive microglia genes (for example, *Stat1*; Fig. 5i–k and Supplementary Table 17)[42]. We confirmed the colocalization of Stat1 protein in Iba1$^+$ cells in lesions of EAE spinal cords (Fig. 5l). M.7 showed an upregulation of growth and ossification pathways and expressed several disease-associated microglia (DAM) marker genes (for example, *Csf1, Lpl, Igf1*), corresponding to a presumed protective microglia state found in several mouse disease models, including Alzheimer's disease (Fig. 5m,n and Supplementary Table 17)[43]. The DAM gene *Spp1* (encodes for osteopontin) has been implicated in both pro-inflammatory and neuroprotective microglia functions[44,45] and is phosphorylated by the simultaneously upregulated kinase *Fam20c*[46]. Immunofluorescence staining revealed Spp1$^+$ cells with high Iba1 expression in and adjacent to EAE lesions (Fig. 5o). Notably, DAM clusters are also present in MS (compare human NucSeq data: M.3 in brain, M.4 in spinal cord; Extended Data Fig. 7e,f)[47].

Collectively, we find that BMT interventions not only decrease the absolute number of immune cells in chronic EAE but also change the composition of subclusters. Although lymphocytes trend towards a normalized distribution pattern, myeloid cells demonstrate an increase in subcluster heterogeneity. This is centered around a further reduction in homeostatic microglia, a rise in cells carrying a CDMC gene signature with probable graft-derived origin (Fig. 6a) and the persistence of DAM.

BMT induces altered myeloid transcriptional profiles

Looking at the underlying DEGs of the EAE myeloid score, it is apparent that the majority of DEGs induced by BMT were conserved—and mostly amplified—in the EAE-BMT-PLX condition (Extended Data Fig. 10d,e). Of note, EAE-BMT-PLX vs EAE DEGs were only partially (64.1%) shared with control vs EAE signature genes and hence only partially reflected in the EAE myeloid score. Strikingly, the different DEG profiles of the two intervention groups indeed demonstrated distinct pathway enrichment patterns (Fig. 6b and Supplementary Table 3). EAE-BMT was characterized by an upregulation of immune pathways such as regulation of cell activation. By contrast, EAE-BMT-PLX induced the upregulation of pathways suggestive for debris-clearing functions such as regulation of autophagy or regulation of hydrolase activity, with associated genes mostly expressed in different subsets of clusters M.6 to M.9 (Fig. 6b). Expression changes of genes associated with EAE-BMT-PLX-induced pathways showed similar directions in EAE-BMT, albeit to a lesser extent. The marker gene profile of subcluster M.6 was specifically associated with catabolic pathways and receptor-mediated endocytosis, suggesting a distinct clearance role of this most likely graft-derived cell population (Fig. 6c and Supplementary Table 17). Pathways enriched for marker genes of clusters M.8 and M.9 were associated with cell signaling and regulation of cell activation.

Together, these results identify altered gene expression profiles in spinal cord myeloid cells that are induced by BMT treatment modalities. Enriched transcriptomic pathways are associated with immune regulation, cell signaling and clearance of debris. These changes are predominantly linked to non-homeostatic myeloid populations.

Iqgap1 expression is elevated in graft-derived myeloid cells

Finally, we sought to visualize and confirm the changes in the myeloid cell phenotype on a histological level. Based on our transcriptomic data, *Iqgap1* (IQ motif containing GTPase activating protein 1) appeared as a suitable marker gene for the subcluster complex M.6 to M.9 (Fig. 6b,d), which represented over half of the myeloid cells in the EAE-BMT-PLX condition (Fig. 5e) and appeared as the main driver population of the above-described transcriptomic changes (Fig. 6b). *Iqgap1* encodes for a cytoplasmic scaffold protein involved in a myriad of cellular functions, including the coordination of signaling events[48]. Of relevance in this context, it has been implicated with a regulatory function in T cell costimulatory receptor OX40 signaling, and a gene knock-out has been reported to exacerbate EAE severity[49]. In addition, it has been identified as an MS GWAS gene (Fig. 1i and Extended Data Fig. 10f) and was expressed in the human brain cluster M.3 in A/CA lesions (Extended Data Fig. 7i)[28].

Our histological findings confirmed that EAE led to a weak expression increase of Iqgap1 in Iba1$^+$ cells that was not further enhanced by the PLX-only treatment (Fig. 6e–g). By contrast, EAE-BMT and—even more prominently—EAE-BMT-PLX induced a marked rise in cells with strong Iqgap1 expression, which colocalized predominantly with GFP$^+$ cells (Fig. 6e,f). Quantification of fluorescence intensity confirmed that graft-derived GFP$^+$ myeloid cells demonstrated higher average expression levels, whereas naive cells maintained expression levels similar between untreated and treated EAE animals (Fig. 6g). Notably, Iqgap1 colocalized with Iba1$^+$ myeloid cells in the murine spinal cord both in EAE lesion areas featuring strong expression as well as being more distant from the surface in ramified cells with moderate expression, while—even though with different frequency and magnitude—being generally detectable in both GFP-derived and graft-derived GFP$^+$ cells (Fig. 6e,f,h). Staining simultaneously for Galectin3 (*Lgals3*), which was robustly expressed in clusters M.7 to M.9 but not M.6 (Fig. 6b), identified Iqgap1$^+$Galectin3$^+$ cells that tended to be located in proximity to the spinal cord border, whereas Iqgap1$^+$ cells more distant from the border were mostly Galectin3$^-$ (Fig. 6h), which is in line with the heterogenous myeloid landscape illustrated by the NucSeq data. Gene expression data suggested that with EAE-BMT and EAE-BMT-PLX, not only the proportion of *Iqgap1* expressing clusters rose but also the expression within these clusters increased (Fig. 6b,d), which is congruent with our histological assessment.

In summary, immunohistological findings confirm an enhancement of *Iqgap1* activity induced by BMT. This additional increase in expression appears mostly restricted to graft-derived cells, suggesting that CDMCs are indeed a main driver of changes in myeloid heterogeneity and associated differential gene expression.

Discussion

Here, we report a comprehensive dataset addressing the chronic stage of EAE, consisting of single-cell level transcriptomics of the murine spinal cord supported by immunohistological and clinical assessment. We found that chronic EAE maintains pathological hallmarks such as demyelinating lesions, reactive astrogliosis and chronic immune cell infiltrations that are accompanied by prominent transcriptional changes and subcluster heterogeneity affecting different lineages. Moreover, we observed certain similarities with human pathobiology, specifically regarding the myeloid response in MS.

We used the chronic EAE model to explore the CNS cell-specific impact of BMT as a model for AHCT in human patients with MS. Although the therapeutic efficacy of AHCT is currently being validated in clinical trials[2], this study provides further preclinical evidence of therapeutic efficacy. Following BMT, oligodendroglial and astroglial cells showed a partial reversion of the transcriptional response to EAE, which was accompanied by enhanced remyelination, reduced reactive astrogliosis and amelioration of paralysis. In stark contrast, the transcriptional response to EAE in spinal cord myeloid cells was further enhanced. To functionally test the role of BMT-derived myeloid cells, we increased their incorporation into the CNS using a microglia replacement protocol[24,25,33–35]. Increased CDMC incorporation further improved clinical paralysis, with a reduction in therapeutic variance compared to the BMT-only approach, and further enhanced the EAE-induced myeloid transcriptional program. At large, these results strongly suggest that the myeloid response in chronic EAE is at least

https://doi.org/10.1038/s41593-024-01609-3

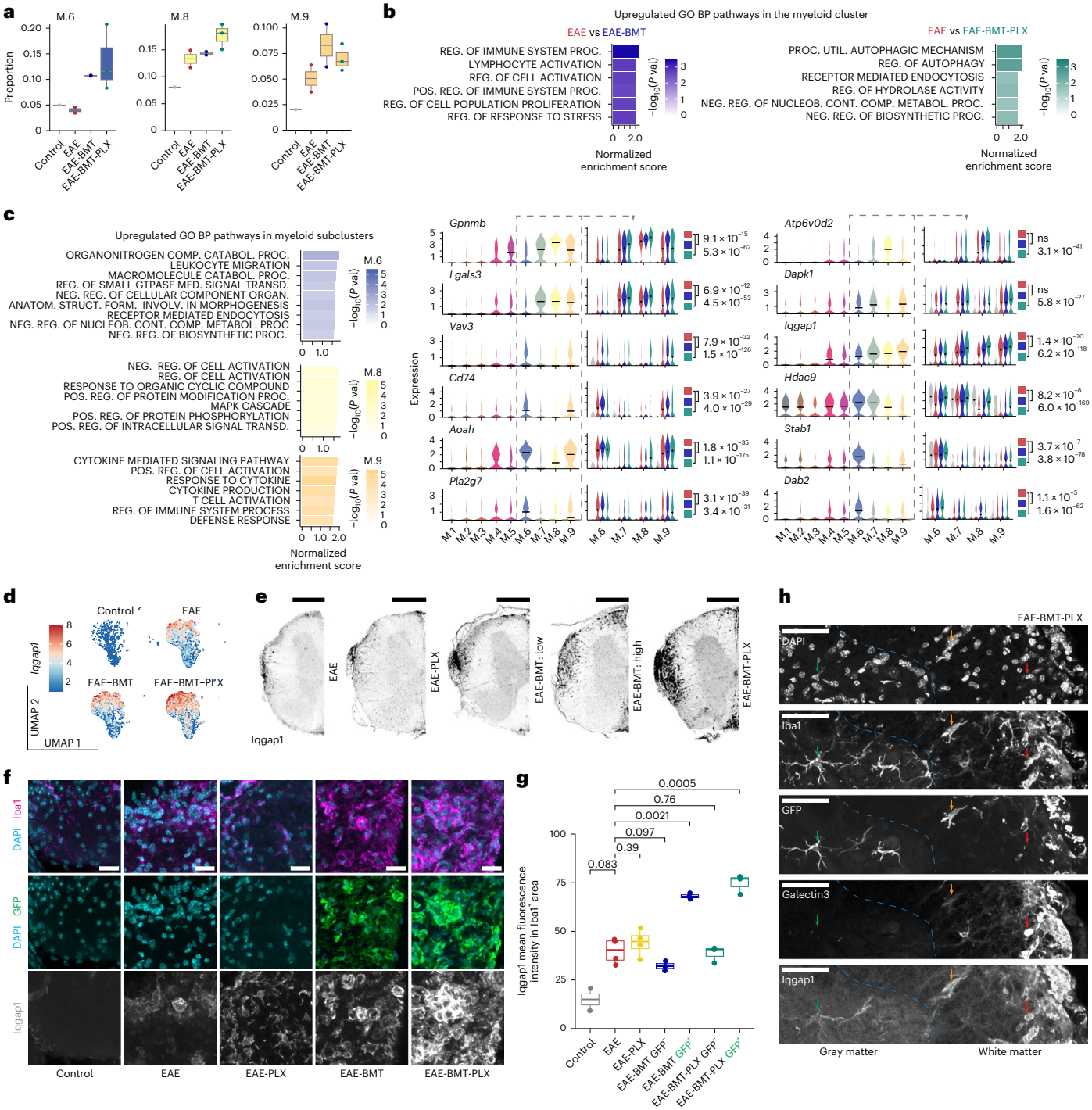


Fig. 6 | Graft-derived Iqgap1$^+$ cells are a main driver of the altered transcriptional state in the CNS myeloid population after BMT. **a**, Relative fractions of selected myeloid subclusters in different conditions ($n = 8$ sequencing libraries derived from 14 animals). **b**, GSEA for the myeloid cluster between the EAE and treatment groups based on DEGs. The top six upregulated GO BP pathways based on GSEA-derived P values are shown (top)[56]. Abbreviations are used for illustrative reasons; the complete list can be found in Supplementary Table 3. Expression of selected leading-edge genes of the bolded pathways in myeloid subclusters and between conditions within subclusters M.6 to M.9 (bottom). Crossbars and diamond markers indicate the median. P_{adj} values are based on the whole myeloid cluster (DEG analysis based on MAST algorithm; see also Supplementary Table 2). Genes indicated as 'ns' were not returned by the DEG analysis. **c**, GSEA based on marker genes of the myeloid subclusters M.6, M.8 and M.9. The top GO BP pathways based on GSEA-derived P values are shown[56]. Abbreviations are used for illustrative reasons; the complete list can be found in Supplementary Table 17. **d**, UMAP of the myeloid subcluster with gene expression of *Iqgap1*. Ordered towards the front based on expression. **e**, Immunofluorescence images of hemi spinal cords stained for Iqgap1 including EAE-BMT animals with low and high GFP$^+$ chimerism. A total of 16 spinal cords were evaluated. Scale bars, 300 µm. **f**, Immunofluorescence images of the subdural white matter of the spinal cord. Scale bars, 20 µm. **g**, Quantification of the mean fluorescence intensity in the Iba1$^+$ area of the spinal cord, distinguished between Iba1$^+$GFP$^-$ and Iba1$^+$GFP$^+$ areas in animals with BMT. Dots show the average of multiple (≥2) spinal cord sections per animal ($n = 16$ animals total). Two-sided Welch t-test. **h**, Immunofluorescence image of spinal cord tissue in an EAE-BMT-PLX animal. Blue dotted line, gray–white matter border. Arrows indicate different protein expression patterns in myeloid cells: GFP$^+$Galectin3$^-$Iqgap1$^+$ (green), GFP$^+$Galectin3$^+$Iqgap1$^+$ (orange), GFP$^-$Galectin3$^+$Iqgap1$^+$ (red). Stain was evaluated in three independent EAE-BMT-PLX spinal cords. Scale bar, 50 µm. Boxplot elements represent the median (center line), first and third quartiles (lower and upper hinges) and smallest and highest values, at most 1.5× the inter-quartile range from the hinge (whiskers).

in part rather neuroprotective, an observation previously made in the context of remyelination[20,21].

Given that the enhanced microglia replacement protocol involves transient CSF1R inhibition, it can be debated whether the beneficial effect observed in this study is truly based on the cellular properties of CDMCs or rather the combination of two separate effects derived from BMT and PLX5622-mediated CSF1R inhibition with microglia depletion. We believe the latter to be unlikely because PLX5622 administration was only transient and of short duration, and is generally followed by rapid repopulation of the myeloid niche[50,51]. Accordingly, we did not detect clinical improvement in the EAE-PLX group. By contrast, early and continuous treatment with a CSF1R inhibitor reduced disease severity in some studies, underlining the relevance of myeloid cells in EAE pathobiology[52–55]. However, drug withdrawal led to a relapse, suggesting that no sustained modulation of the myeloid niche was achieved[54]. These results, in light of the findings of our study, demonstrate that the role of myeloid cells is complex. Firstly, there appear to be opposing roles of CNS-resident and circulation-derived myeloid subpopulations. Secondly, the role of CNS myeloid cells might change over time with a contribution to neuroinflammation early in EAE but exertion of a restorative function in the chronic phase[19–21].

Collectively, our findings identify manipulation of the myeloid niche as a therapeutic direction for inflammatory demyelinating disease. Our data supports the notion that the combination of CSF1R inhibition with AHCT might have translational implications, warranting further exploration of the specific role and mechanisms of replaced myeloid cells in the context of inflammatory CNS disease.

Online content

Any methods, additional references, Nature Portfolio reporting summaries, source data, extended data, supplementary information, acknowledgements, peer review information; details of author contributions and competing interests; and statements of data and code availability are available at https://doi.org/10.1038/s41593-024-01609-3.

References

1. Wallin, M. T. et al. Global, regional, and national burden of multiple sclerosis 1990–2016: a systematic analysis for the Global Burden of Disease Study 2016. *Lancet Neurol.* **18**, 269–285 (2019).
2. Miller, A. E. et al. Autologous hematopoietic stem cell transplant in multiple sclerosis: recommendations of the national multiple sclerosis society. *JAMA Neurol.* **78**, 241–246 (2021).
3. Noseworthy, J. H., Lucchinetti, C., Rodriguez, M. & Weinshenker, B. G. Multiple sclerosis. *N. Engl. J. Med.* **343**, 938–952 (2000).
4. Yong, H. Y. F. & Yong, V. W. Mechanism-based criteria to improve therapeutic outcomes in progressive multiple sclerosis. *Nat. Rev. Neurol.* **18**, 40–55 (2022).
5. Mancardi, G. L. et al. Autologous hematopoietic stem cell transplantation in multiple sclerosis: a phase II trial. *Neurology* **84**, 981–988 (2015).
6. Nash, R. A. et al. High-dose immunosuppressive therapy and autologous hematopoietic cell transplantation for relapsing-remitting multiple sclerosis (HALT-MS): a 3-year interim report. *JAMA Neurol.* **72**, 159–169 (2015).
7. Atkins, H. L. et al. Immunoablation and autologous haemopoietic stem-cell transplantation for aggressive multiple sclerosis: a multicentre single-group phase 2 trial. *Lancet* **388**, 576–585 (2016).
8. Moore, J. J. et al. Prospective phase II clinical trial of autologous haematopoietic stem cell transplant for treatment refractory multiple sclerosis. *J. Neurol. Neurosurg. Psychiatry* **90**, 514–521 (2019).
9. Burt, R. K. et al. Effect of nonmyeloablative hematopoietic stem cell transplantation vs continued disease-modifying therapy on disease progression in patients with relapsing–remitting multiple sclerosis: a randomized clinical trial. *JAMA* **321**, 165–174 (2019).
10. Muraro, P. A. et al. Thymic output generates a new and diverse TCR repertoire after autologous stem cell transplantation in multiple sclerosis patients. *J. Exp. Med.* **201**, 805–816 (2005).
11. Muraro, P. A. et al. T cell repertoire following autologous stem cell transplantation for multiple sclerosis. *J. Clin. Invest.* **124**, 1168–1172 (2014).
12. Massey, J. et al. Haematopoietic stem cell transplantation results in extensive remodelling of the clonal T cell repertoire in multiple sclerosis. *Front. Immunol.* **13**, 798300 (2022).
13. Ruder, J. et al. Dynamics of T cell repertoire renewal following autologous hematopoietic stem cell transplantation in multiple sclerosis. *Sci. Transl. Med.* **14,** eabq1693 (2022).
14. Gold, R. Understanding pathogenesis and therapy of multiple sclerosis via animal models: 70 years of merits and culprits in experimental autoimmune encephalomyelitis research. *Brain* **129**, 1953–1971 (2006).
15. Psenicka, M. W., Smith, B. C., Tinkey, R. A. & Williams, J. L. Connecting neuroinflammation and neurodegeneration in multiple sclerosis: Are oligodendrocyte precursor cells a nexus of disease? *Front. Cell. Neurosci.* **15**, 654284 (2021).
16. Williams, J. L. et al. Astrocyte–T cell crosstalk regulates region-specific neuroinflammation. *Glia* **68**, 1361–1374 (2020).
17. Meijer, M. et al. Epigenomic priming of immune genes implicates oligodendroglia in multiple sclerosis susceptibility. *Neuron* **110**, 1193–1210.e13 (2022).
18. Ajami, B. et al. Single-cell mass cytometry reveals distinct populations of brain myeloid cells in mouse neuroinflammation and neurodegeneration models. *Nat. Neurosci.* **21**, 541–551 (2018).
19. Guerrero, B. L. & Sicotte, N. L. Microglia in multiple sclerosis: Friend or foe? *Front. Immunol.* **11**, 374 (2020).
20. Miron, V. E. et al. M2 microglia and macrophages drive oligodendrocyte differentiation during CNS remyelination. *Nat. Neurosci.* **16**, 1211–1218 (2013).
21. Lampron, A. et al. Inefficient clearance of myelin debris by microglia impairs remyelinating processes. *J. Exp. Med.* **212**, 481–495 (2015).
22. Falcão, A. M. et al. Disease-specific oligodendrocyte lineage cells arise in multiple sclerosis. *Nat. Med.* **24**, 1837–1844 (2018).
23. Jordão, M. J. C. et al. Single-cell profiling identifies myeloid cell subsets with distinct fates during neuroinflammation. *Science* **363**, eaat7554 (2019).
24. Sailor, K. A. et al. Hematopoietic stem cell transplantation chemotherapy causes microglia senescence and peripheral macrophage engraftment in the brain. *Nat. Med.* **28**, 517–527 (2022).
25. Shibuya, Y. et al. Treatment of a genetic brain disease by CNS-wide microglia replacement. *Sci. Transl. Med.* **14**, eabl9945 (2022).
26. DeTomaso, D. et al. Functional interpretation of single cell similarity maps. *Nat. Commun.* **10**, 4376 (2019).
27. Hahn, O. et al. Atlas of the aging mouse brain reveals white matter as vulnerable foci. *Cell* **186**, 4117–4133.e22 (2023).
28. International Multiple Sclerosis Genetics Consortium et al. Multiple sclerosis genomic map implicates peripheral immune cells and microglia in susceptibility. *Science* **365**, eaav7188 (2019).
29. Trobisch, T. et al. Cross-regional homeostatic and reactive glial signatures in multiple sclerosis. *Acta Neuropathol.* **144**, 987–1003 (2022).
30. Absinta, M. et al. A lymphocyte–microglia–astrocyte axis in chronic active multiple sclerosis. *Nature* **597**, 709–714 (2021).
31. Schirmer, L. et al. Neuronal vulnerability and multilineage diversity in multiple sclerosis. *Nature* **573**, 75–82 (2019).
32. Jäkel, S. et al. Altered human oligodendrocyte heterogeneity in multiple sclerosis. *Nature* **566**, 543–547 (2019).

33. Hohsfield, L. A. et al. Effects of long-term and brain-wide colonization of peripheral bone marrow-derived myeloid cells in the CNS. *J. Neuroinflammation* **17**, 279 (2020).
34. Xu, Z. et al. Efficient strategies for microglia replacement in the central nervous system. *Cell Rep.* **32**, 108041 (2020).
35. Cronk, J. C. et al. Peripherally derived macrophages can engraft the brain independent of irradiation and maintain an identity distinct from microglia. *J. Exp. Med.* **215**, 1627–1647 (2018).
36. Lee, H. K. et al. Daam2-PIP5K Is a regulatory pathway for Wnt signaling and therapeutic target for remyelination in the CNS. *Neuron* **85**, 1227–1243 (2015).
37. Liddelow, S. A. et al. Neurotoxic reactive astrocytes are induced by activated microglia. *Nature* **541**, 481–487 (2017).
38. Escartin, C. et al. Reactive astrocyte nomenclature, definitions, and future directions. *Nat. Neurosci.* **24**, 312–325 (2021).
39. Haimon, Z. et al. Cognate microglia–T cell interactions shape the functional regulatory T cell pool in experimental autoimmune encephalomyelitis pathology. *Nat. Immunol.* **23**, 1749–1762 (2022).
40. Van Hove, H. et al. A single-cell atlas of mouse brain macrophages reveals unique transcriptional identities shaped by ontogeny and tissue environment. *Nat. Neurosci.* **22**, 1021–1035 (2019).
41. Bennett, F. C. et al. A combination of ontogeny and CNS environment establishes microglial identity. *Neuron* **98**, 1170–1183.e8 (2018).
42. Hammond, T. R. et al. Single-cell RNA sequencing of microglia throughout the mouse lifespan and in the injured brain reveals complex cell-state changes. *Immunity* **50**, 253–271.e6 (2019).
43. Keren-Shaul, H. et al. A unique microglia type associated with restricting development of Alzheimer's disease. *Cell* **169**, 1276–1290.e17 (2017).
44. Shen, X., Qiu, Y., Wight, A. E., Kim, H.-J. & Cantor, H. Definition of a mouse microglial subset that regulates neuronal development and proinflammatory responses in the brain. *Proc. Natl Acad. Sci.* **119**, e2116241119 (2022).
45. Schroeter, M., Zickler, P., Denhardt, D. T., Hartung, H.-P. & Jander, S. Increased thalamic neurodegeneration following ischaemic cortical stroke in osteopontin-deficient mice. *Brain* **129**, 1426–1437 (2006).
46. Tagliabracci, V. S. et al. A single kinase generates the majority of the secreted phosphoproteome. *Cell* **161**, 1619–1632 (2015).
47. Masuda, T. et al. Spatial and temporal heterogeneity of mouse and human microglia at single-cell resolution. *Nature* **566**, 388–392 (2019).
48. Abel, A. M. et al. IQGAP1: insights into the function of a molecular puppeteer. *Mol. Immunol.* **65**, 336–349 (2015).
49. Okuyama, Y. et al. IQGAP1 restrains T-cell cosignaling mediated by OX40. *FASEB J.* **34**, 540–554 (2020).
50. Huang, Y. et al. Repopulated microglia are solely derived from the proliferation of residual microglia after acute depletion. *Nat. Neurosci.* **21**, 530–540 (2018).
51. Elmore, M. R. P. et al. Colony-stimulating factor 1 receptor signaling is necessary for microglia viability, unmasking a microglia progenitor cell in the adult brain. *Neuron* **82**, 380–397 (2014).
52. Hwang, D. et al. CSF-1 maintains pathogenic but not homeostatic myeloid cells in the central nervous system during autoimmune neuroinflammation. *Proc. Natl Acad. Sci.* **119**, e2111804119 (2022).
53. Hagan, N. et al. CSF1R signaling is a regulator of pathogenesis in progressive MS. *Cell Death Dis.* **11**, 904 (2020).
54. Nissen, J. C., Thompson, K. K., West, B. L. & Tsirka, S. E. Csf1R inhibition attenuates experimental autoimmune encephalomyelitis and promotes recovery. *Exp. Neurol.* **307**, 24–36 (2018).
55. Wlodarczyk, A. et al. CSF1R stimulation promotes increased neuroprotection by $CD11c^{+}$ microglia in EAE. *Front. Cell. Neurosci.* **12**, 523 (2019).
56. Korotkevich, G. et al. Fast gene set enrichment analysis. Preprint at https://doi.org/10.1101/060012 (2021).

Publisher's note Springer Nature remains neutral with regard to jurisdictional claims in published maps and institutional affiliations.

Springer Nature or its licensor (e.g. a society or other partner) holds exclusive rights to this article under a publishing agreement with the author(s) or other rightsholder(s); author self-archiving of the accepted manuscript version of this article is solely governed by the terms of such publishing agreement and applicable law.

© The Author(s), under exclusive licence to Springer Nature America, Inc. 2024

Methods

Animal procedures

Female C57BL/6J mice were used for the EAE model (JAX, strain 000664). The C57BL/6-Tg(UBC-GFP)30Scha/J strain (JAX, strain 004353) was crossed with wild-type C57BL/6J mice to generate hemizygote UBC-GFP animals. Female 10–12-week-old hemizygote UBC-GFP mice were used as donor animals for BMT. All animal procedures were approved by the administrative panel on laboratory animal care at Stanford University (APLAC21565). Mice were group-housed (up to five mice per cage) on a 12:12 h light:dark cycle with water and standard chow provided ad libitum unless otherwise described below. The ambient temperature was 20–22 °C and humidity was 20–80%. Animals were randomly assigned to experimental groups.

Experimental autoimmune encephalitis

EAE was induced using the Hooke Kit $MOG_{35–55}$/CFA Emulsion PTX (Hooke Laboratories, EK-2110) according to the manufacturer's instructions in female C57BL/6J mice at the age of 11 weeks. On day 0, animals received a percutaneous injection of 100 µl in two sites (total of 200 µl) of the antigen emulsion of $MOG_{35–55}$ in CFA. This was followed by an intraperitoneal injection of 110 ng pertussis toxin (PTX) after 2 h (in 100 µl volume of freshly prepared solution from a 200 ng $µl^{-1}$ stock solution, diluted in cold PBS). The preparation and injection of PTX solution was repeated after 24 h. Injections were carried out under isoflurane sedation. Animals without clinical presentation (clinical score = 0) were excluded from the experiment before the initiation of any therapeutic measures. In the early stages of the disease, and later in cages for animals with clinical scores of ≥3.0, additional gel food was provided (DietGel Boost, ClearH_2O). Additional supportive care was provided to animals with a clinical score of >3.0 in the form of subcutaneous saline injection. Animals that died before day 50 were excluded from the analysis. The observation period was either 3 months for animals used for NucSeq or 4 months for spinal cord histological analysis. CFA control animals for the NucSeq control cohort were injected with CFA without $MOG_{35–55}$ (Hooke Laboratories, CK-2110).

Clinical scoring

The clinical evaluation was performed blinded for the experimental groups. Clinical scoring was applied according to the manufacturer's instructions (Hooke Kit, Hooke Laboratories, EK-2110). In brief, a scale from 0–5 with increments of 0.5 was used. Most relevant clinical presentations are no obvious motor deficits, a limp tail, weakness of hind legs, complete paralysis of hind legs, additional partial front leg paralysis and death owing to severity of symptoms, which correspond to scores of 0, 1, 2, 3, 4 and 5, respectively. A detailed table is provided by the manufacturer (https://hookelabs.com/protocols/eaeAI_C57BL6.html). Animals that were killed for animal welfare reasons unrelated to EAE severity were excluded from the analysis after the timepoint of their death.

Busulfan conditioning and bone marrow transplantation

Busulfan (Sigma-Aldrich, B2635) conditioning was started after peak disease severity on day 20 after EAE induction. A working solution of 1 mg ml^{-1} was prepared fresh every day from a DMSO stock solution of 49 mg ml^{-1} by dilution with PBS. Busulfan was applied intraperitoneally with a daily dose of 25 mg kg^{-1} over five subsequent days. Non-BMT EAE animals received injections with PBS. BMT was performed on day 25. UBC-GFP donor mice were killed with CO_2. Tibias and femurs were pestled in ice-cold PBS to collect the bone marrow. The cell solution was then filtered through a 70 µm cell strainer and spun down for 5 min at 350×*g*. The cell pellet was washed one time in ice-cold PBS, cell number was counted and cells were again resuspended in ice-cold PBS. Preconditioned recipient mice were retro-orbitally injected with five million bone marrow cells in 200 µl PBS.

PLX5622 treatment

PLX5622 was provided by Plexxikon Inc. under a material transfer agreement and incorporated into AIN-76A standard chow by Research Diets Inc. at 1,200 parts per million. Mice were treated with PLX5622 or control diet ad libitum from day 41 until day 50 after EAE induction. Chow was placed both in the food reservoir of the cage and on the cage floor to allow easy access for paralyzed animals.

Immunofluorescence staining and microscopy

The following primary antibodies were used for immunofluorescence staining: C4 (abcam, ab11863; 1:100), CD206 (R&D systems, AF2535; 1:40), Galectin-3 (Mac-2, Biolegend, 125401; 1:100), GFAP (Invitrogen, 13-0300; 1:500), GFP (abcam, ab13970; 1:1,000), Iba1 (FUJIFILM Wako, 019-19741; 1:1,000), Iba1 (abcam, ab5076; 1:500), IQGAP1 (abcam, ab133490; 1:50 or 1:100), NLRC5 (abcam ab105411; 1:200), Olig2 (Millipore Sigma, AB9610; 1:1,000), Spp1 (Santa Cruz Biotechnology, sc-21742; 1:40) and Stat1 (Cell Signaling, 14994; 1:200). Tissue collection for immunofluorescent analysis was performed 4 months after EAE induction or in age-matched healthy control animals. Animals were anesthetized (Avertin, Sigma-Aldrich, T48402) and transcardially perfused with ice-cold PBS followed by 4% PFA before collecting the brain and spinal cord. NucSeq animals were killed 3 months after EAE induction, perfused with ice-cold PBS and brains were drop-fixed in 4% PFA. All tissues were fixed in 4% PFA for 18 h at 4 °C. Tissues were then moved into a 30% sucrose in PBS solution, embedded with Tissue-Tek OCT compound (Sakura Finetek, 4583) and sections of 40 µm were obtained using a cryostat (CM 3050S, Leica). After washing with PBS, sections were incubated in IF buffer (PBS with 5% cosmic calf serum and 0.3% Triton X-100; Sigma-Aldrich) for 1 h. If FluoroMyelin Red fluorescent myelin stain (Invitrogen, F34652) was used, sections were incubated with FluoroMyelin 1:300 in PBS for 30 min after the blocking step and subsequently washed in PBS. Primary and secondary antibodies were diluted in IF buffer. Primary antibody staining was performed at 4 °C overnight. Sections were subsequently washed three times in PBS. Secondary antibody (ThermoFisher) stain was performed at room temperature (20–21 °C) for 1 h. Fluorophores included Alexa Fluor 488, 594, 647 and 750. Sections were subsequently washed three times in PBS and counterstained with DAPI for 5 min. Sections were washed once with PBS and mounted on glass slides with ProLong Gold antifade reagent (ThermoFisher, P36930). Images were obtained using a Zeiss LSM710 confocal microscope, Zeiss AxioImager motorized widefield fluorescence microscope or Leica DMi8 using consistent imaging parameters per stain. Five-channel imaging was obtained with a Zeiss LSM980 with near infrared imaging. For image acquisition, ZEN blue (Zeiss, v.3.7.97.04000), Zen black (Zeiss, v.14.0.28.201) and Leica Application Suite X (LAS X, Leica, v.3.7.4.23463 and v.3.5.7.23225) software applications were used.

Image analysis and quantification

Image postprocessing and analyses were performed using ImageJ (National Institutes of Health, USA) software. Postprocessing workflow and parameters were kept consistent per stain unless otherwise stated. For chimerism and myeloid density, images were taken using a fluorescence microscope. For the brain, ×10 images were taken from the cortex, hippocampus and cerebellum, sampling between two and four sections per region. For the spinal cord, tiled images were taken from axial thoracic and lumbar cords. Quantification of chimerism and myeloid density was performed manually using the CellCounter plugin. Percent chimerism was determined by GFP^+Iba1^+ cells divided by total $Iba1^+$ cells. For the density of myeloid cells, total $Iba1^+$ cells were divided by area of region of interest. For FluoroMyelin analysis, tiled fluorescent images were taken from axial cervical, lumbar and thoracic spinal cord sections. All stained spinal cords were imaged and analyzed, resulting in two to six sections per replicate per anatomical region. Quantifications were performed blinded. To quantify the percentage

of demyelination, boundaries were manually drawn around areas of demyelination at the edge of the spinal cord, which was defined as regions with DAPI$^+$FluoroMyelin$^-$ staining and divided by total white matter area, which was defined by total spinal cord area minus gray matter area. For GFAP analysis, tiled fluorescent images were taken from axial thoracic and lumbar spinal cord with two to four sections per anatomical region per replicate. Images were converted into 8-bit grayscale, and total GFAP area was obtained using a set lower signal boundary applied using the standard threshold plugin. The GFAP$^+$ area was normalized by dividing the value by the total spinal cord area. For branch analysis, confocal images of microglia and CDMCs were obtained from spinal cord gray matter and cortex at ×40, Z-stack of 25 µm at 1 µm Z-interval. Brightness and contrast were optimized to allow for visualization of morphology owing to variations in Iba1 staining related to the treatment condition. Images were converted into 8-bit grayscale and processed using standard plugins (that is, despeckle, FTT bandpass, thresholding, unsharp mask, despeckle, close, skeletonize). Skeletonized images were analyzed using the Analyze Skeleton plugin. For quantification of CD206 expression, spinal cord sections were co-stained for Iba1, CD206, GFP and DAPI. Whole spinal cord sections were analyzed per condition. Regions of interest included white matter and border-associated (within two cell bodies outside the outer rim of the spinal cord) Iba1$^+$ cells. Imaging acquisition was performed on confocal microscopy and standardized between all images. On ImageJ, masks were created using Iba1 staining and applied to the channel with CD206 staining to measure CD206 average intensity for individual cells. For BMT and BMT-PLX conditions, Iba1$^+$ cells were also separately analyzed by GFP$^+$ or GFP$^-$ labeling to assess differential CD206 expression between the two populations. For quantification of Iqgap1, spinal cords were co-stained for Iqgap1, GFP and Iba1. Images were acquired using confocal microscopy using standardized acquisition settings. At least two whole spinal cord sections were quantified per condition. Using ImageJ, separate masks were created for GFP$^+$ and GFP$^-$ Iba1 cells. Each mask was applied to the Iqgap1 channel to calculate the average intensity of Iqgap1 immunofluorescence of the whole spinal cord.

Peripheral blood analysis and flow cytometry

Peripheral blood was collected from the facial vein and treated with 0.5 M EDTA. Erythrocytes were removed by 10 min of incubation in 2 ml ice-cold RBC lysis buffer[57]. Cells were collected by centrifugation for 10 min at 300×*g*. Cells were washed with PBS and then stained for 15 min at 4 °C in flow buffer (PBS with 5% cosmic calf serum) containing the antibodies CD11b-PE (Invitrogen, 12-0112-82; 1:200) and CD45-APC (Biolegend, 103112; 1:200). Stained cells were washed in PBS and resuspended in flow buffer with DAPI (Sigma, D9542). Flow cytometry was performed on a FACS AriaII. Data analysis was performed using FlowJo software. The percentage of GFP$^+$ cells within the CD45$^+$CD11b$^+$ live population was determined.

Isolation of nuclei from frozen spinal cord tissue

Tissue collection for the transcriptomic analysis was performed 3 months after EAE induction or in an age-matched healthy control animal for the main cohort (14 animals). Healthy control animals that received PBS vehicle injections and were age-matched to the main cohort (four animals), and animals 25 days after injection of CFA and PTX without $MOG_{35–55}$ (four animals) were used for a second control cohort (Hooke Laboratories, CK-2110). Animals were anesthetized (Avertin, Sigma-Aldrich, T48402) and transcardially perfused. Spinal cords were collected by hydraulic expulsion and snap-frozen by submerging for 60 s in liquid nitrogen-cooled isopentane. Frozen spinal cords were stored at −80 °C until further processing. Single-nuclei preparation was performed as previously described with the following modifications[58]. The thoracolumbar sections of spinal cords were first mechanically dissociated with an ice-cold razor blade in a Petri dish with 1 ml EZ Prep lysis buffer (Sigma, NUC-101) on ice. The tissue suspension was transferred into a 2 ml glass Dounce tissue grinder tube (Sigma, D8938). The Petri dish was rinsed off with another 1 ml EZ buffer, which was added to the grinder tube. The suspension was then homogenized by hand 25 times with pestle A followed by 25 times with pestle B while incorporating a 180° twist. The tissue homogenate was transferred to a fresh 15 ml tube on ice. The grinder tube was rinsed with 2 ml fresh lysis buffer, which was added to the 15 ml tube for a total volume of 4 ml. Samples were incubated on ice for 5 min. Nuclei were centrifuged at 500×*g* for 5 min at 4 °C, the supernatant was removed and the pellet resuspended with 4 ml EZ lysis buffer and incubated on ice for 5 min, and centrifugation at 500×*g* for 5 min at 4 °C was repeated. After removing the supernatant, the pellet was resuspended with 4 ml chilled PBS and filtered through a 35 µm cell strainer into a 5 ml round-bottom FACS tube (Corning, 352235). Following centrifugation at 300×*g* for 10 min at 4 °C with break setting 3, the supernatant was gently poured out, leaving behind the nuclei pellet. The pellet was resuspended in 100 µl FC block buffer (BD Biosciences, 553141; 1:50 in FACS buffer) and 1 µl recombinant RNase inhibitor (Takara, 2313B) and then incubated on ice for 5 min. The FACS buffer consisted of PBS (Gibco, 10010049) containing 1% BSA (ThermoFisher, BP9700100). To 50 µl of the cell suspension, we added 150 µl FACS buffer with 2 µl Olig2-AlexaFluor488 (Sigma, MABN50A4), 1 µl NeuN-AlexaFluor647 (Abcam, ab190565) and 1.5 µl RNase inhibitor. Anti-Nuclear Pore Complex Protein Hashtag antibodies (1 µl) was additionally added to the samples of the control cohort (TotalSeq-A0451, TotalSeq-A0452, TotalSeq-A0453 and TotalSeq-A0455; Biolegend, 682205, 682207, 682209 and 682213). After 30 min incubation while being covered from light and shaking on ice, 3 ml FACS buffer was added. Following centrifugation at 300×*g* for 10 min at 4 °C with break setting 3, the supernatant was gently poured out. The pellet was resuspended in 700 µl FACS buffer with 3.5 µl recombinant RNase inhibitor and Hoechst dye (ThermoFisher, H357; 1:2000) and incubated for 4 min on ice, covered from light. Single nuclei were sorted on an MA900 Multi-Application Cell Sorter (Sony Biotechnology) gating for NeuN$^-$ nuclei. An aliquot of 100,000 single nuclei per sample was collected into 1.5 ml DNA lo-bind tubes (Eppendorf, 022431021) containing 1 ml buffer mix with 800 µl PBS, 200 µl UltraPure BSA (ThermoFisher, AM2618) and 5 µl RNase inhibitor. If libraries represented two or more animals, samples were pooled by collecting identical numbers (2 × 50,000 or 4 × 25,000) of nuclei from the same condition into the same sample tube. Collected nuclei were centrifuged at 400×*g* for 5 min at 4 °C with break setting 2. Then the supernatant was removed, leaving 40 µl suspended nuclei. The nuclei were counted using a hemacytometer (Sigma, Z359629-1EA) and assessed for concentration and quality.

Droplet-based NucSeq

Reagents of the Chromium Next GEM Single Cell 3′ GEM & Gel Bead Kit v.3.1 (10× Genomics, 1000128) were thawed and prepared according to the manufacturer's protocol. The nuclei and master mix solution was adjusted to target 10,000 nuclei per sample and loaded on a standard Chromium Controller (10× Genomics, 1000204) according to the manufacturer's protocols. We applied 11 PCR cycles to generate cDNA. Library construction was conducted using the Chromium Next GEM Single Cell 3′ Library Kit v.3.1 (10× Genomics, 1000128). All reaction and quality control steps were carried out according to the manufacturer's protocol and with recommended reagents, consumables and instruments. We chose 11 PCR cycles for library generation. Quality control of cDNA and libraries was conducted using a bioanalyzer (Agilent) at the Stanford Protein and Nucleic Acid Facility. For the main cohort, Illumina sequencing of the resulting libraries was performed by Novogene (https://en.novogene.com/) on an Illumina NovaSeq S4 (Illumina). Base calling, demultiplexing and generation of FastQ files were conducted by Novogene. For the control cohort, libraries were prepared according to the 10× manufacturer protocol as described

above, with the addition of HTO additive primer at cDNA amplification. A total of 11 PCR cycles were applied to generate cDNA. Immediately after cDNA amplification, HTO-derived cDNA and mRNA-derived cDNA were separated by SPRI bead size selection. Generation of libraries for the mRNA-derived cDNA was carried out as described above, using 13 PCR cycles. The HTO-derived cDNA was processed according to the New York Genome Center Cell Hashing Protocol (https://citeseq.files.wordpress.com/2019/02/cell_hashing_protocol_190213.pdf) with 13 PCR cycles. Libraries were pooled at a proportion of 20% HTO-derived cDNA to 80% mRNA-derived cDNA. Sequencing of the libraries was conducted using an Illumina NextSeq 550 (Illumina). Base calling, demultiplexing and generation of FastQ files for the control cohort data was conducted using the mkfastq command of the 10× Genomics Cell Ranger software (v.6.1.2).

Mapping, integration, quality control, clustering, annotation and subclustering of NucSeq data (main cohort)

The 10× Genomics Cell Ranger (v.6.1.2) analysis pipelines were used to align reads to the mm10 reference genome as well as *GFP* and count barcodes or unique molecular identifiers. The nucleotide sequence for *GFP* was retrieved by Sanger sequencing (Supplementary File 1) of a PCR product generated from genomic DNA of a C57BL/6-Tg(UBC-GFP)30Scha/J mouse with the following primer pair: forward CTTTAGTTGCAAGGGTTTCTG and reverse ATCAACTTTC-CTGTGCGTAGG, which was based on previous mapping[59]. To account for unspliced nuclear transcripts, reads mapping to pre-mRNA were counted. Separate Seurat objects were created per library, including features expressed by at least a minimum of three cells and including cells with expression of at least 50 features. Outliers with a ratio of mitochondrial relative to endogenous RNAs of >5%, homotypic doublets (>6,000 features) and debris (<400 features) were removed after inspection of data distribution. We integrated all eight Seurat objects, using Seurat's built-in SCTransform and integration workflow with 2,000 genes set as integration features[60,61]. The integrated dataset was used as input for cell embedding and clustering. A shared-nearest-neighbors graph was constructed using the first 20 PC dimensions before clustering spots using Seurat's built-in FindClusters function with a resolution of 0.6 and default parameters. Uniform manifold approximation and projection (UMAP) plots were calculated using Seurat's built-in functions, based on the first 20 PC dimensions. Count data were subsequently normalized and scaled to allow for visualization of expression values and differential gene expression analysis. Seurat's FindAllMarkers function (with default statistical test (Wilcoxon rank sum test) and the following parameters: only.pos = TRUE, min.pct = 0.15, logfc.threshold = 0.15, assay = 'SCT') was run to identify cluster markers. Clusters were annotated based on canonical marker genes derived from previous publications[23,42,62–65]. Nuclei clusters were manually inspected for debris and doublet clusters, which were removed for downstream analysis. Clusters expressing more than one cell type-specific marker signature were defined as doublets. For subclustering, new Seurat objects were generated from clusters of the main integrated dataset with Seurat's subset function. Each new object was reintegrated using the SCTransform-based workflow with subsequent clustering as outlined above. Clustering parameters were 15 PC dimensions and a resolution of 0.6 for immune cells (combined main clusters 'myeloid' and 'lymphocytes') and 10 PC dimensions and a resolution of 0.4 for astrocytes. Downstream processing including the removal of doublet subclusters, and annotation was performed as described above. Further subclustering for T cells from the immune cell subcluster was performed with 15 PC dimensions and a resolution of 1.2, followed by the removal of a small cluster with Schwann cell signature. An average expression matrix was generated with the built-in Seurat function AverageExpression (layer = 'data') for visualization in the Shiny app (created with the R package shiny v.0.61.1), which can be accessed at https://werniglab.shinyapps.io/scthi/.

Mapping, integration, quality control, clustering, annotation and subclustering of NucSeq data (control cohort)

NucSeq data analysis for the control cohort was performed as outlined above for the main cohort with the following adaptions. Cell demultiplexing by assigning hashtag antibody oligo tags to cell-associated barcodes was performed with the 10× Genomics Cell Ranger multi pipeline. The resulting per-sample matrices were used to generate separate Seurat objects (four objects per library, eight objects total), including features expressed by at least a minimum of three cells and including cells with expression of at least 50 features. Outliers with a ratio of mitochondrial relative to endogenous RNAs of >5%, homotypic doublets (>4,000 features) and debris (<500 features) were removed after inspection of the data distribution. The eight Seurat objects were integrated using Seurat's built-in SCTransform[60,61]. Clustering (20 PC dimensions, resolution of 0.6) and annotation were performed as described above.

Differential gene expression analysis and gene set enrichment analysis

Differential gene expression analysis comparing the different experimental groups was performed for each of the main 12 clusters of the main integrated NucSeq dataset and the immune subclusters, as well as for the ten main clusters of the control cohort. For oligodendrocyte lineage and astrocyte clusters, differential gene expression analysis was performed subsequent to the removal of a respective doublet subcluster (subcluster analysis with ten PC dimensions and a resolution of 0.4 for both; details see above). Calculations were based on the MAST algorithm[66] with a log(fold change) threshold of 0.25, minimum detection fraction of 0.1 and Bonferroni correction of *P* values. DEGs were considered significant at $P_{adj} < 0.05$. We compared the resulting DEGs with the murine ortholog of genes derived from a human MS GWAS study (see Supplementary Table 4)[28]. Gene set enrichment analysis was performed using the fgsea package (v.1.24.0) for Gene Ontology terms, hallmark and KEGG pathways; genes were ranked based on $\log_2$(fold change) expression, and pathways with 15 to 500 genes were considered[56].

Gene signature score calculation

The generation of gene signature scores was performed using the VISION (v.3.0) package as detailed in the original study, using default settings without pooling and signed signatures[26]. VISION *z*-normalizes signature scores with random gene signatures to account for global sample-level metrics. Gene signatures can be found in Supplementary Table 4.

Analysis of human spinal cord NucSeq data

A previously published human spinal cord dataset was accessed from the Sequence Read Archive (accession number PRJNA726991)[29] as six fastq files (three control and three MS samples). The 10× Genomics Cell Ranger (v.6.1.2) analysis pipelines were used to align reads to the GRCh38 reference genome. Separate Seurat objects were created per library, including features expressed by at least a minimum of three cells and including cells with expression of at least 50 features. Outliers with a ratio of mitochondrial relative to endogenous RNAs of >5% were removed. Thresholds for features, based on inspection of the separate objects, were as follows: SRR14408223: >150 and <1,500; SRR14408224, SRR14408225, SRR14408231, SRR14408232: >300 and <3,000; and SRR14408226: >200 and <2,000. We integrated all six objects, using Seurat's built-in SCTransform and integration workflow with 2,000 genes set as integration features[60,61]. The integrated dataset was used as input for cell embedding and clustering. A shared-nearest-neighbors graph was constructed using the first 12 PC dimensions before clustering spots using Seurat's built-in FindClusters function with a resolution of 0.4 and default parameters. UMAPs were calculated using Seurat's built-in functions, based on the first 12 PC dimensions. Count data

was subsequently normalized and scaled to allow for visualization of expression values and differential gene expression analysis. Seurat's FindAllMarkers function (with default statistical test (Wilcoxon rank sum test) and the following parameters: only.pos = TRUE, min.pct = 0.15, logfc.threshold = 0.15, assay = 'SCT') was run to identify cluster markers. Clusters were annotated based on canonical marker genes[29]. No debris or doublet clusters were detected at this level. Differential gene expression analysis was based on the MAST algorithm[66] with a log(fold change) threshold of 0.25, minimum detection fraction of 0.1 and Bonferroni correction of *P* values. DEGs were considered significant at $P_{adj} < 0.05$. Expression of the EAE scores, based on a signed signature of the human orthologs, was calculated using the VISION package without pooling and with default settings[26]. Immune cells were subclustered by sub-setting the 'myeloid' and 'lymphocyte' clusters, followed by reintegration and clustering as described above, with clustering parameters of 15 PC dimensions and a resolution of 0.8. Subclusters with relevant expression of non-immune cell marker genes were excluded for downstream analysis.

Analysis of human brain NucSeq data

Data from previously published human brain NucSeq datasets ((three control and five MS samples)[30]; (five control and four MS samples)[32]; and (nine control and twelve MS samples)[31]) were obtained as expression matrices from the UCSC Cell Browser (https://cells.ucsc.edu)[67]. For one dataset[31], nuclei with a maximum number of 10,000 features were used and duplicated gene symbols were kept as distinct genes. No further adaptions were made to the other two datasets before integration. We integrated the datasets using Seurat's built-in SCTransform and integration workflow with 2,000 genes set as integration features[60,61]. The integrated dataset was used as input for cell embedding and clustering. A shared-nearest-neighbors graph was constructed using the first 20 PC dimensions before using Seurat's built-in FindClusters function with a resolution of 0.6 and default parameters. UMAPs were calculated using Seurat's built-in functions, based on the first 20 PC dimensions. Count data was subsequently normalized and scaled to allow for visualization of expression values and differential gene expression analysis. Seurat's FindAllMarkers function (with the default statistical test (Wilcoxon rank sum test) and the following parameters: only.pos = TRUE, min.pct = 0.15, logfc.threshold = 0.15, assay = 'SCT') was run to identify cluster markers. Nuclei clusters were manually inspected for doublet clusters, which were removed for downstream analysis. Differential gene expression analysis was based on the MAST algorithm[66] with a log(fold change) threshold of 0.25, minimum detection fraction of 0.1 and Bonferroni correction of *P* values. DEGs were considered significant at $P_{adj} < 0.05$. Expression of the EAE myeloid score, based on a signed signature of the human orthologs, was calculated from the unique molecular identifier-scaled expression matrix using the VISION package without pooling and with default settings[26]. Immune cells were subclustered by sub-setting the 'myeloid' and 'lymphocyte' clusters, followed by reintegration and clustering as described above, with clustering parameters of 15 PC dimensions and a resolution of 0.4. Subclusters with relevant expression of non-immune cell marker genes were excluded for downstream analysis.

Statistical analyses

No statistical methods were used to pre-determine sample sizes but our sample sizes are similar to those reported in previous publications[22,42,47]. Statistical tests were chosen based on the type and distribution of data and are specified in the figure legends or the respective method sections above. Data distribution was not formally tested but was assessed based on visual inspection of data points. Handling and presentation of data and statistical analyses were performed in the R programming language (v.4.1.2 and v.4.2.0) with the RStudio interface, using open-source packages including dplyr (v.1.10.0), tidyr (v.1.2.1), ggplot2 (v.3.4.0), ggpubr (v.0.5.0), UpSetR (v.1.4.0), VennDiagram (v.1.7.3), ggrepel (v.0.9.2), Seurat (v.4.2.0)[68], biomaRt (v.2.50.3)[69], sctransform (v.0.3.5)[61], fgsea (v.1.24.0)[56], MAST (v.1.20.0)[66] and VISION (v.3.0.0)[26]. A level of significance of 5% was chosen. The final figures were designed using Adobe Illustrator (v.28.1).

Reporting summary

Further information on research design is available in the Nature Portfolio Reporting Summary linked to this article.

Data availability

The murine sequencing datasets generated and analyzed in the current study are available in the Gene Expression Omnibus repository under accession numbers GSE217529 and GSE242512. The human spinal cord dataset[29] was accessed as six fastq files (three control and three MS samples) through Sequence Read Archive (accession number PRJNA726991). Data from previously published human brain NucSeq datasets ((three control and five MS samples; Cell Browser dataset ID, chronic-ms)[30]; (five control and four MS samples; Cell Browser dataset ID, oligodendrocyte-ms)[32]; and (nine control and twelve MS samples; Cell Browser dataset ID, ms)[31]) were obtained as expression matrices from the UCSC Cell Browser (https://cells.ucsc.edu)[67]. Reference genomes (refdata-gex-mm10-2020-A and refdata-gex-GRCh38-2020-A) were accessed at www.10xgenomics.com. Source data are provided with this paper.

Code availability

Computational analyses were performed using freely available software packages as described in the Methods. Central to the analysis pipeline of NucSeq data in this study are the software packages 10× Genomics Cell Ranger (v.6.1.2; https://www.10xgenomics.com/support/software/cell-ranger)[70] and R packages Seurat (v.4.2.0)[68], sctransform (v.0.3.5)[61], fgsea (v.1.24.0)[56], MAST (v.1.20.0)[66], VISION (v.3.0.0)[26] and biomaRt (v.2.50.3)[69]. Additional information regarding the computational methodology of this project is available from the corresponding author upon reasonable request.

References

57. Cold Spring Harbor Protocols. Red blood cell lysis buffer. *Cold Spring Harbor Protocols* 2006:db.rec390 (2006).
58. Hahn, O. et al. CoolMPS for robust sequencing of single-nuclear RNAs captured by droplet-based method. *Nucleic Acids Res.* **49**, e11 (2021).
59. Liu, S., Lockhart, J. R., Fontenard, S., Berlett, M. & Ryan, T. M. Mapping the chromosomal insertion site of the GFP transgene of UBC-GFP mice to the MHC locus. *J. Immunol.* **204**, 1982–1987 (2020).
60. Stuart, T. et al. Comprehensive integration of single-cell data. *Cell* **177**, 1888–1902.e21 (2019).
61. Hafemeister, C. & Satija, R. Normalization and variance stabilization of single-cell RNA-seq data using regularized negative binomial regression. *Genome Biol.* **20**, 296 (2019).
62. Russ, D. E. et al. A harmonized atlas of mouse spinal cord cell types and their spatial organization. *Nat. Commun.* **12**, 5722 (2021).
63. Blum, J. A. et al. Single-cell transcriptomic analysis of the adult mouse spinal cord reveals molecular diversity of autonomic and skeletal motor neurons. *Nat. Neurosci.* **24**, 572–583 (2021).
64. Zeisel, A. et al. Molecular architecture of the mouse nervous system. *Cell* **174**, 999–1014.e22 (2018).
65. Marques, S. et al. Oligodendrocyte heterogeneity in the mouse juvenile and adult central nervous system. *Science* **352**, 1326–1329 (2016).
66. Finak, G. et al. MAST: a flexible statistical framework for assessing transcriptional changes and characterizing heterogeneity in single-cell RNA sequencing data. *Genome Biol.* **16**, 278 (2015).

67. Speir, M. L. et al. UCSC Cell Browser: visualize your single-cell data. *Bioinformatics* **37**, 4578–4580 (2021).
68. Hao, Y. et al. Integrated analysis of multimodal single-cell data. *Cell* **184**, 3573–3587.e29 (2021).
69. Durinck, S., Spellman, P. T., Birney, E. & Huber, W. Mapping identifiers for the integration of genomic datasets with the R/Bioconductor package biomaRt. *Nat. Protoc.* **4**, 1184–1191 (2009).
70. Zheng, G. X. Y. et al. Massively parallel digital transcriptional profiling of single cells. *Nat. Commun.* **8**, 14049 (2017).

Acknowledgements

We would like to thank all members of the Wernig laboratory, G. Wang, C. Bennett, B. Ajami, J. Blum and N. Or-Geva for helpful discussions throughout the project; A. Lang and M. Vangipuram for administrative support; and the FACS core at the Institute for Stem Cell Biology and Regenerative Medicine and Stanford Neuroscience Microscopy Service (supported by the National Institutes of Health, NS069375) for technical support. We thank the scientists at Plexxikon Inc. for their generous gift of PLX5622. Funding was provided by a Howard Hughes Medical Institute Faculty Scholar Award (to M.W.); the German Research Foundation (Deutsche Forschungsgemeinschaft; MA 8492/1-1 to M.M.D.M.); the National Multiple Sclerosis Society and the American Brain Foundation (FAN-2207-39823 to D.W.); and the New York Stem Cell Foundation Druckenmiller Fellowship (NYSCF-D-F74 to Y.Y.).

Author contributions

M.M.D.M., M.W., L.S., R.D. and C.T. designed and conceived the study. M.M.D.M., A.N., Y.S., A.S., D.W., Y.Y., R.D. and C.T. worked with the study animals. M.M.D.M., M.A., A.F., O.H. and T.W.C. performed the NucSeq experiments and analysis. D.W., A.S., M.M.D.M. and A.N. performed immunostaining, microscopy and image analysis. M.M.D.M., M.W., O.H., A.N., D.W. and L.S. performed data analysis and interpretation. M.M.D.M. and M.W. drafted and edited the original manuscript; all authors reviewed, revised and approved the final version of the paper.

Competing interests

The authors declare that they have no conflict of interest related to this study. PLX5622 was provided by Plexxikon Inc. under a material transfer agreement between Stanford University and Plexxikon Inc.

Additional information

Extended data is available for this paper at https://doi.org/10.1038/s41593-024-01609-3.

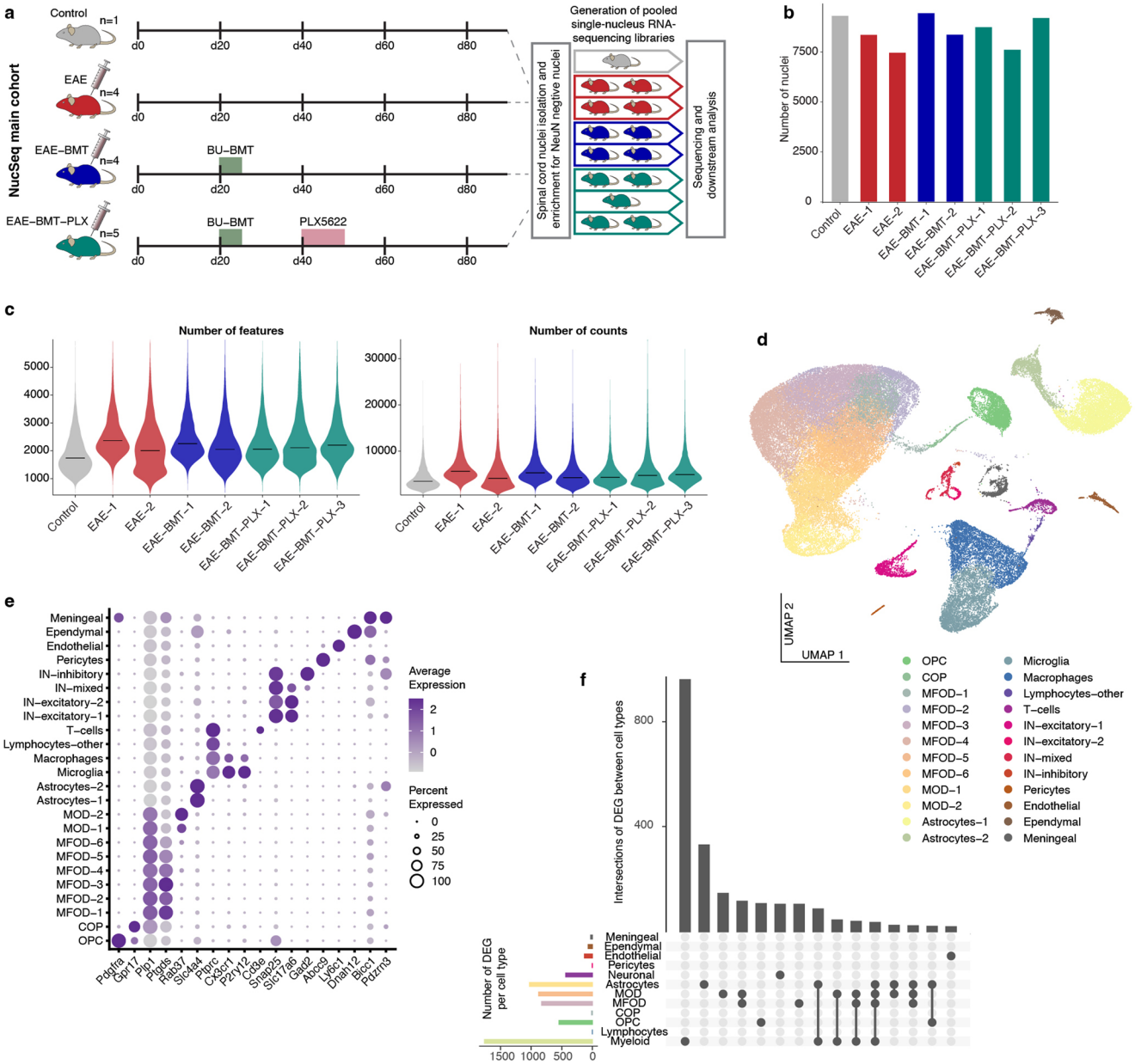
Supplementary information The online version contains supplementary material available at https://doi.org/10.1038/s41593-024-01609-3.

Correspondence and requests for materials should be addressed to Marius Wernig.

Peer review information *Nature Neuroscience* thanks Jessica Williams and the other, anonymous, reviewer(s) for their contribution to the peer review of this work.

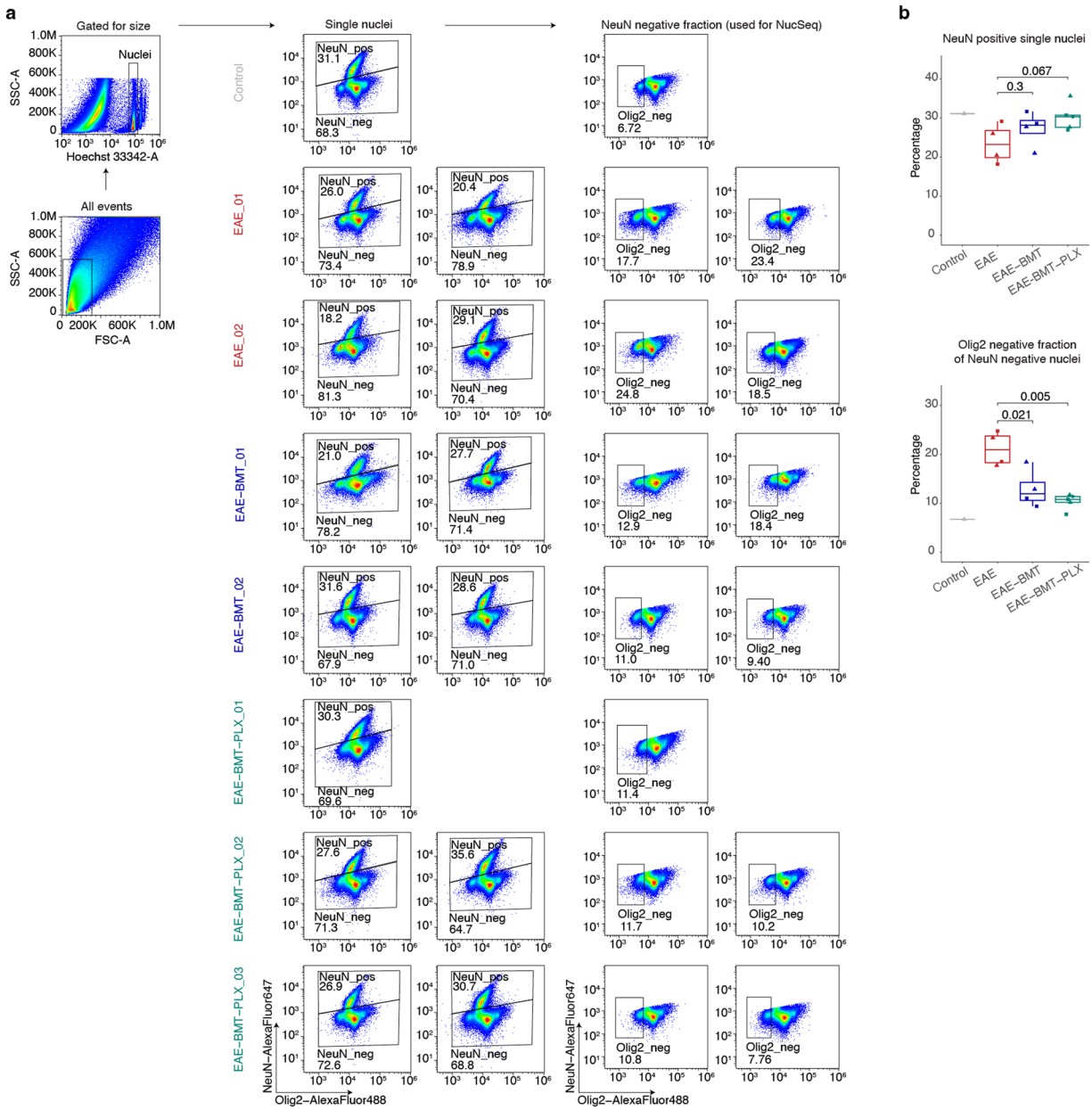
Reprints and permissions information is available at www.nature.com/reprints.

https://doi.org/10.1038/s41593-024-01609-3



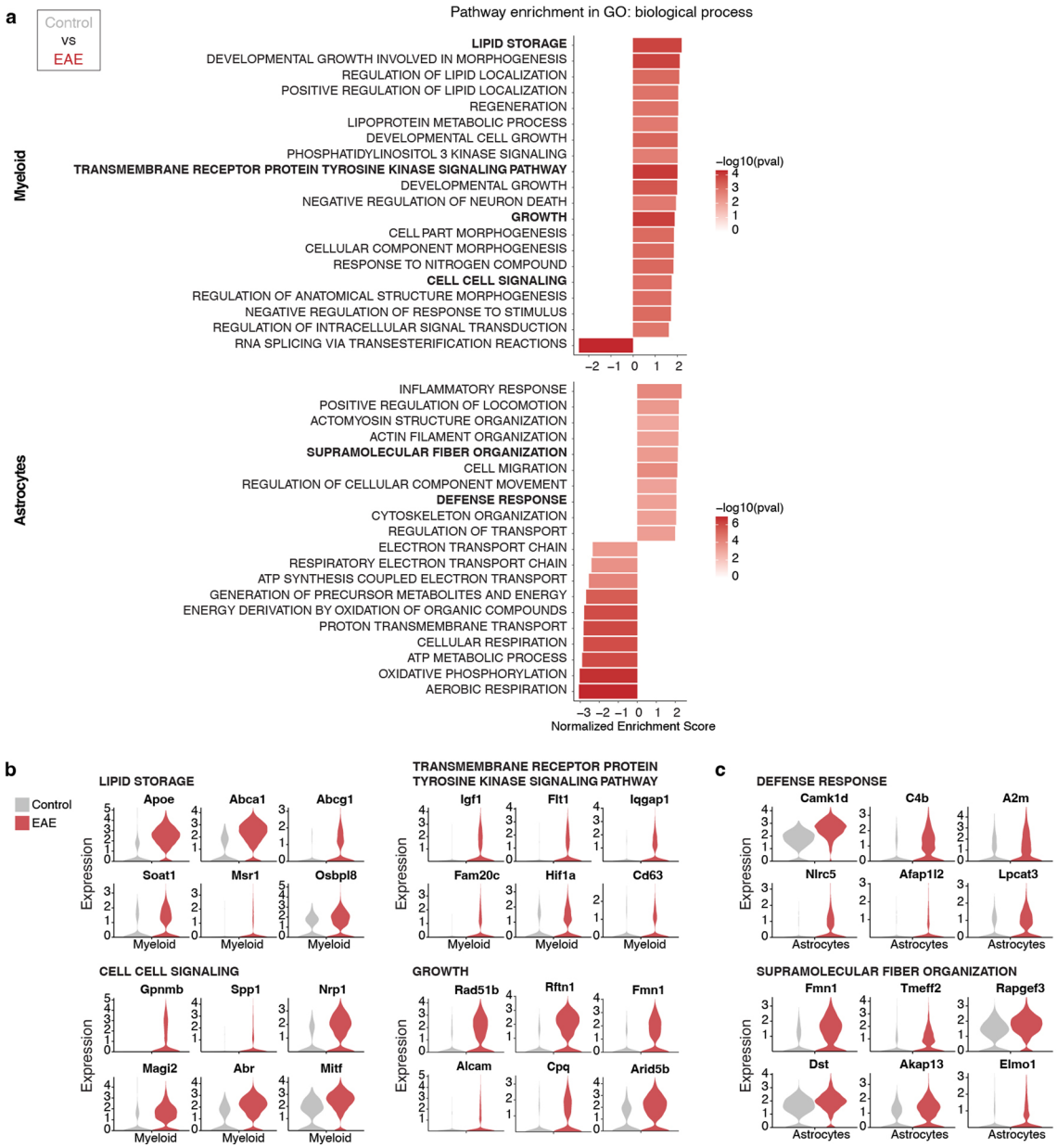
Extended Data Fig. 1 | Characterization of chronic EAE via spinal cord NucSeq. a, Experimental design and groups of the NucSeq main cohort. **b**, Absolute number of nuclei per library. **c**, Number of features and counts per library. **d**, Annotated UMAP plot of 68,593 nuclei integrated from all 8 libraries. Clustering based on the first 20 principal components and a resolution of 0.6. **e**, Annotation and canonical marker genes of clusters. **f**, Significant DEGs (padj < 0.05, based on MAST) for main cell types between the *Control* and *EAE* condition. The top 15 intersections are illustrated.

https://doi.org/10.1038/s41593-024-01609-3



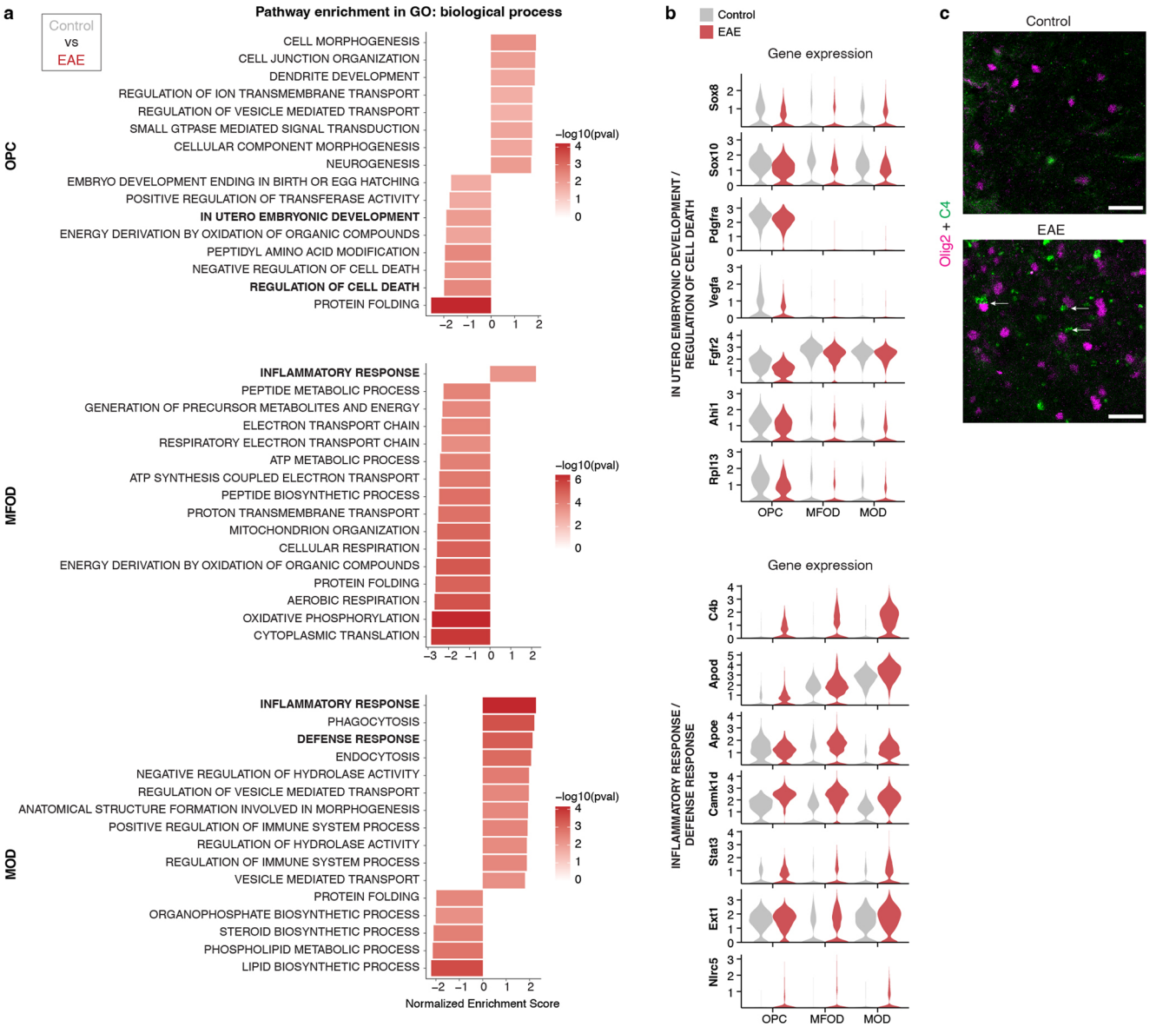
Extended Data Fig. 2 | Flowcytometric analysis of murine spinal cord nuclei reveals an increase in the NeuN- Olig2- fraction in EAE. a, Gating strategy of fluorescence activated nuclei sorting and representative gates for each animal. **b**, Quantification of gated populations. Two-sided Welch t-test. Total n = 14 animals. Box plot elements represent median (center line), first and third quartiles (lower and upper hinges) and smallest/highest value with at most 1.5*IQR (inter-quartile range) from the hinge (whiskers).

https://doi.org/10.1038/s41593-024-01609-3



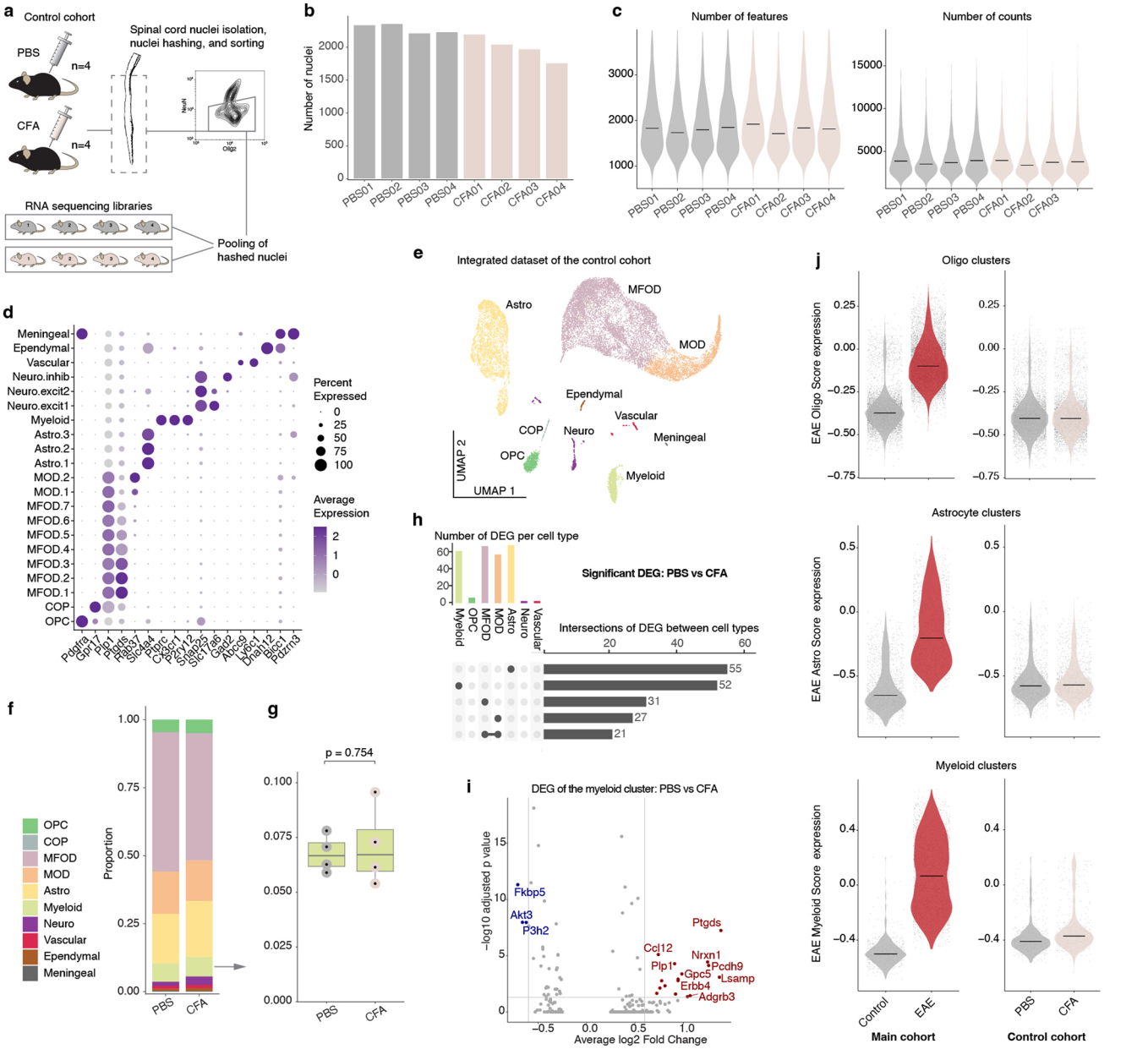
Extended Data Fig. 3 | EAE alters the transcriptional program in both astrocytes and myeloid cells. a, GSEA-derived top 20 significantly enriched pathways (*Control* vs *EAE*) of the Gene Ontology biological process term for the myeloid and astrocyte clusters (p values based on GSEA). **b, c**, Representative genes of selected enriched pathways.

https://doi.org/10.1038/s41593-024-01609-3



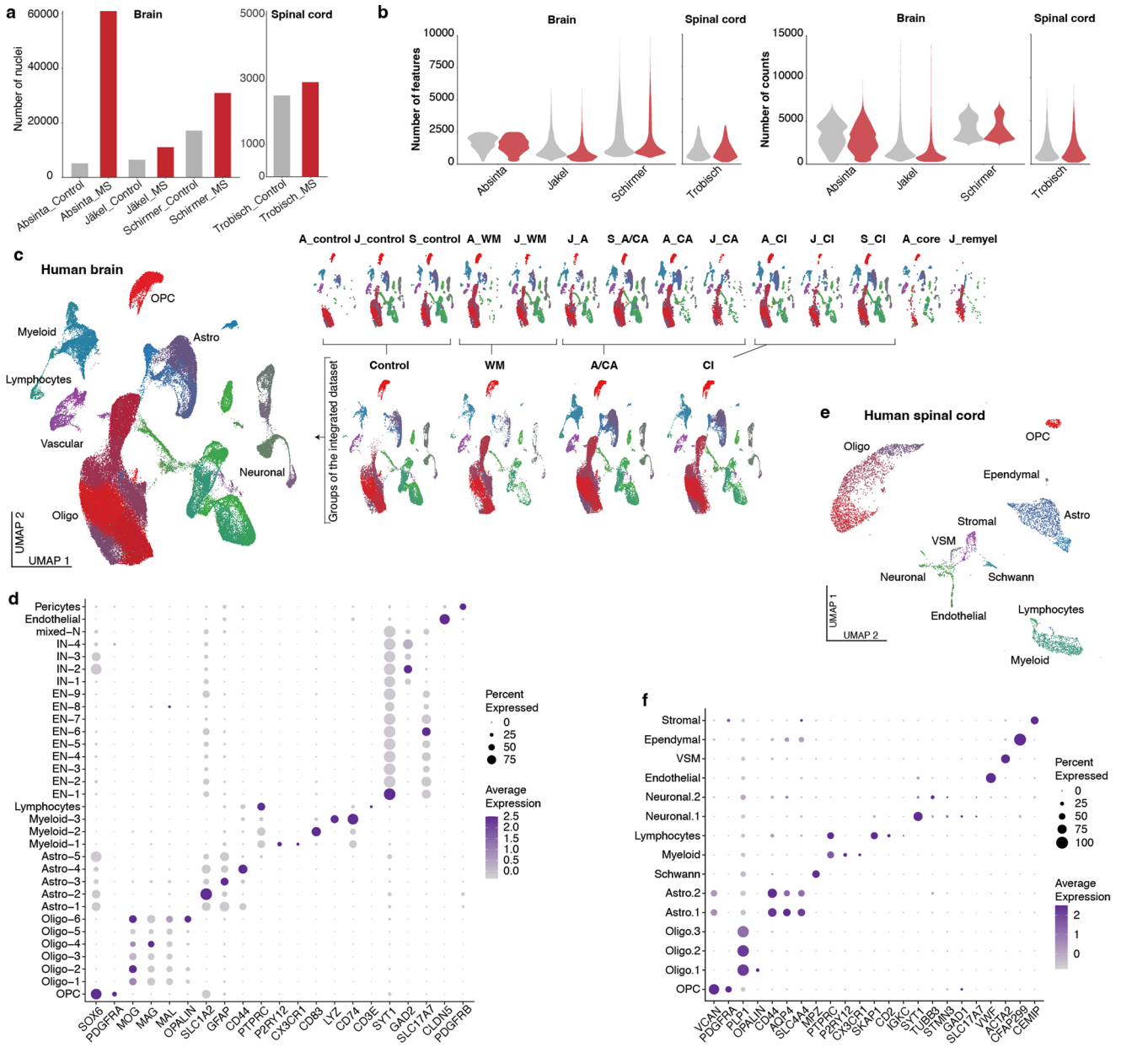
Extended Data Fig. 4 | EAE induces a proinflammatory gene set enrichment in oligodendrocytes. a, GSEA-derived top 16 significantly enriched pathways (*Control* vs *EAE*) of the Gene Ontology biological process term for oligodendrocyte lineage clusters (p values based on GSEA). **b**, Representative genes of selected enriched pathways. **c**, Immunofluorescent stain for Olig2 and complement component 4 (C4) in the spinal cord white matter. White arrows demonstrate spatial association between C4 and oligodendrocytes. Stain was evaluated in three independent *EAE* and three independent *Control* spinal cords. Scale bar is 20 µm.

https://doi.org/10.1038/s41593-024-01609-3



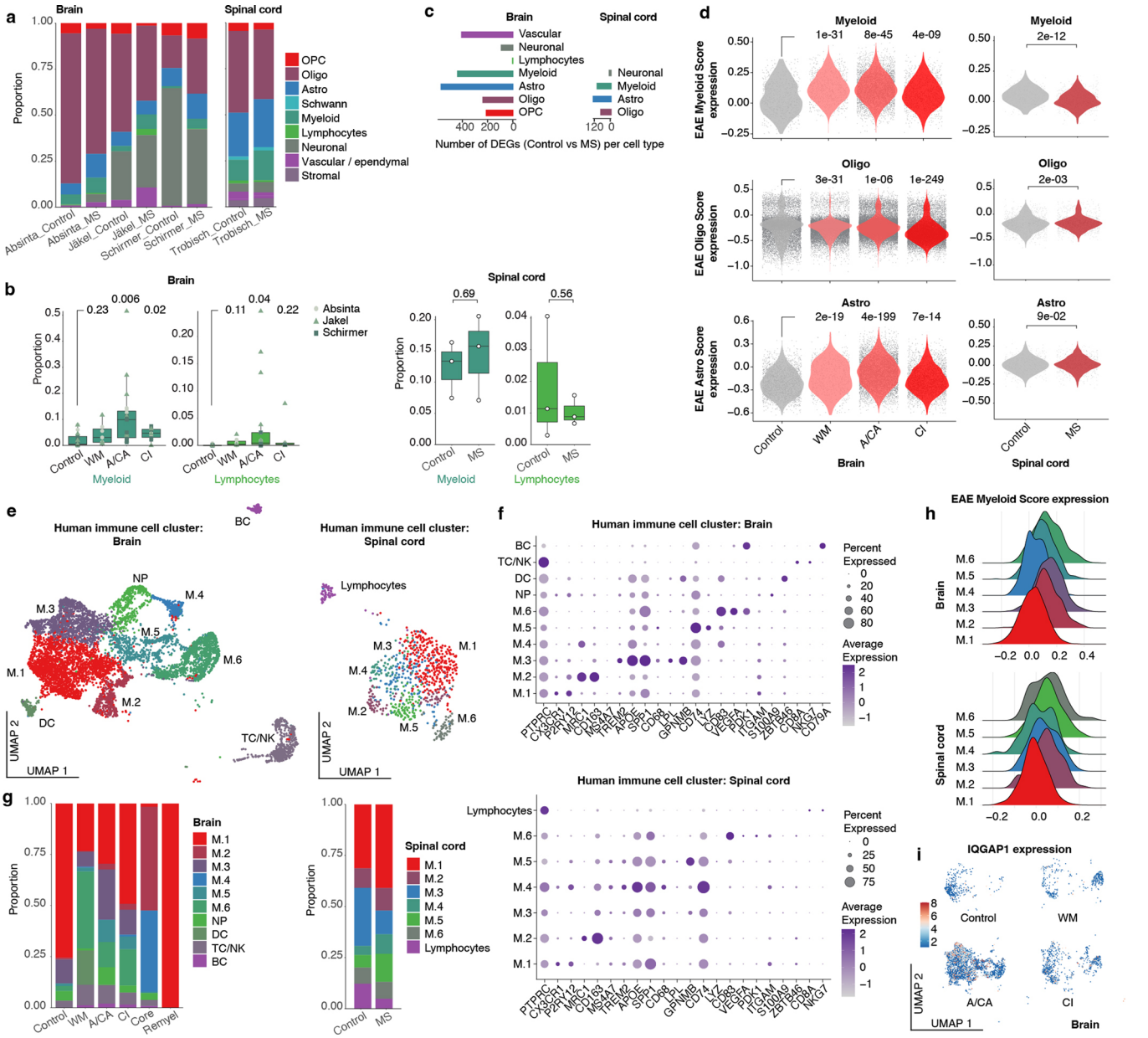
Extended Data Fig. 5 | EAE-specific transcriptional changes are not induced by CFA injection without MOG-immunization. a, Experimental design of the control cohort. Animals with Complete Freund's Adjuvant (CFA) were sacrificed and analyzed 25 days after injection. Animals injected with phosphate buffered saline (PBS) were age matched to the animals of the main cohort at the timepoint of analysis. **b**, Absolute number of nuclei per animal sample. **c**, Number of features and counts per animal sample. **d**, Annotation and canonical marker genes of cell clusters. Clustering based on the first 20 principal components and a resolution of 0.6. **e**, UMAP plot of 17,127 nuclei integrated from the murine control cohort. **f**, Distribution of main cell clusters of the PBS and CFA groups. **g**, Fraction of myeloid nuclei. Dots represent individual animals (n = 8 animals total). Two-sided Welch t-test. **h**, Absolute number and top five intersections of significant DEGs (padj < 0.05) between PBS and CFA group. **i**, DEGs of the myeloid cluster between PBS and CFA group. Significant (padj < 0.05) genes are color coded if >1.5 fold up (red) or down (blue) regulated. **j**, Expression of EAE Scores in *Control* and *EAE* animals of the main cohort (left panels), and PBS and CFA animals of the control cohort (right panels). Box plot elements represent median (center line), first and third quartiles (lower and upper hinges) and smallest/highest value with at most 1.5*IQR (inter-quartile range) from the hinge (whiskers).

https://doi.org/10.1038/s41593-024-01609-3



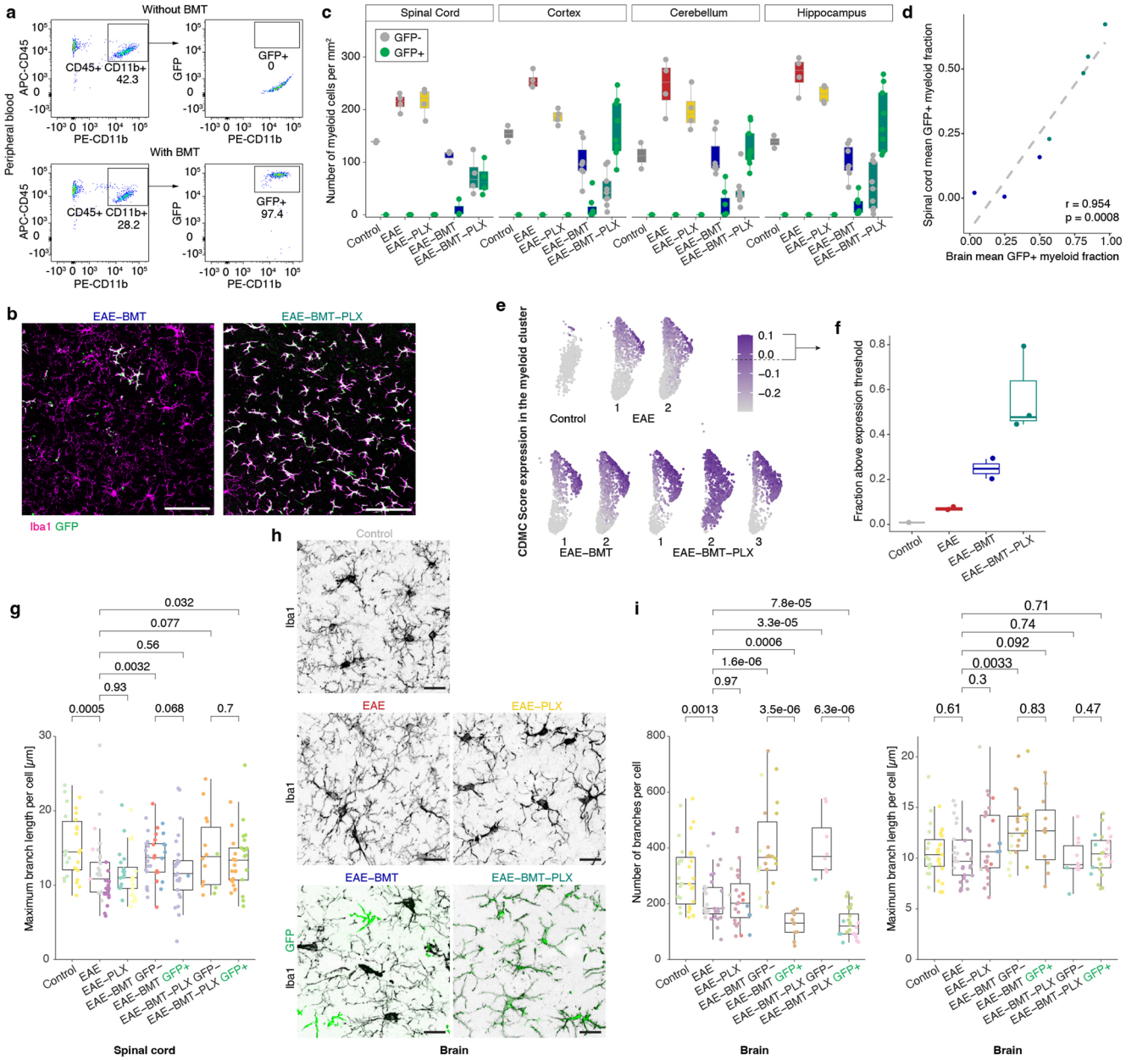
Extended Data Fig. 6 | Integration of NucSeq data derived from MS patients. **a**, Absolute number of nuclei per original human dataset. **b**, Number of features and counts per original human dataset. **c**, UMAP plot of 132,425 nuclei integrated from the original human brain datasets. Lesion-dependent conditions of the original datasets are shown (A_, Absinta; J_, Jäkel; S_, Schirmer; A, active; A/CA, acute/chronic active; CA, chronic active; CI, chronic inactive; remyel, remyelinating; wm, white matter), which were combined into 4 groups: control, active/chronic active (A/CA), chronic inactive (CI), and MS white matter (WM). **d**, Annotation and canonical marker genes of brain clusters. Clustering based on the first 12 principal components and a resolution of 0.4. **e**, UMAP plot of 5419 nuclei integrated from the original individual libraries derived from human spinal cord samples. **f**, Annotation and canonical marker genes of spinal cord clusters. Clustering based on the first 12 principal components and a resolution of 0.4.

https://doi.org/10.1038/s41593-024-01609-3



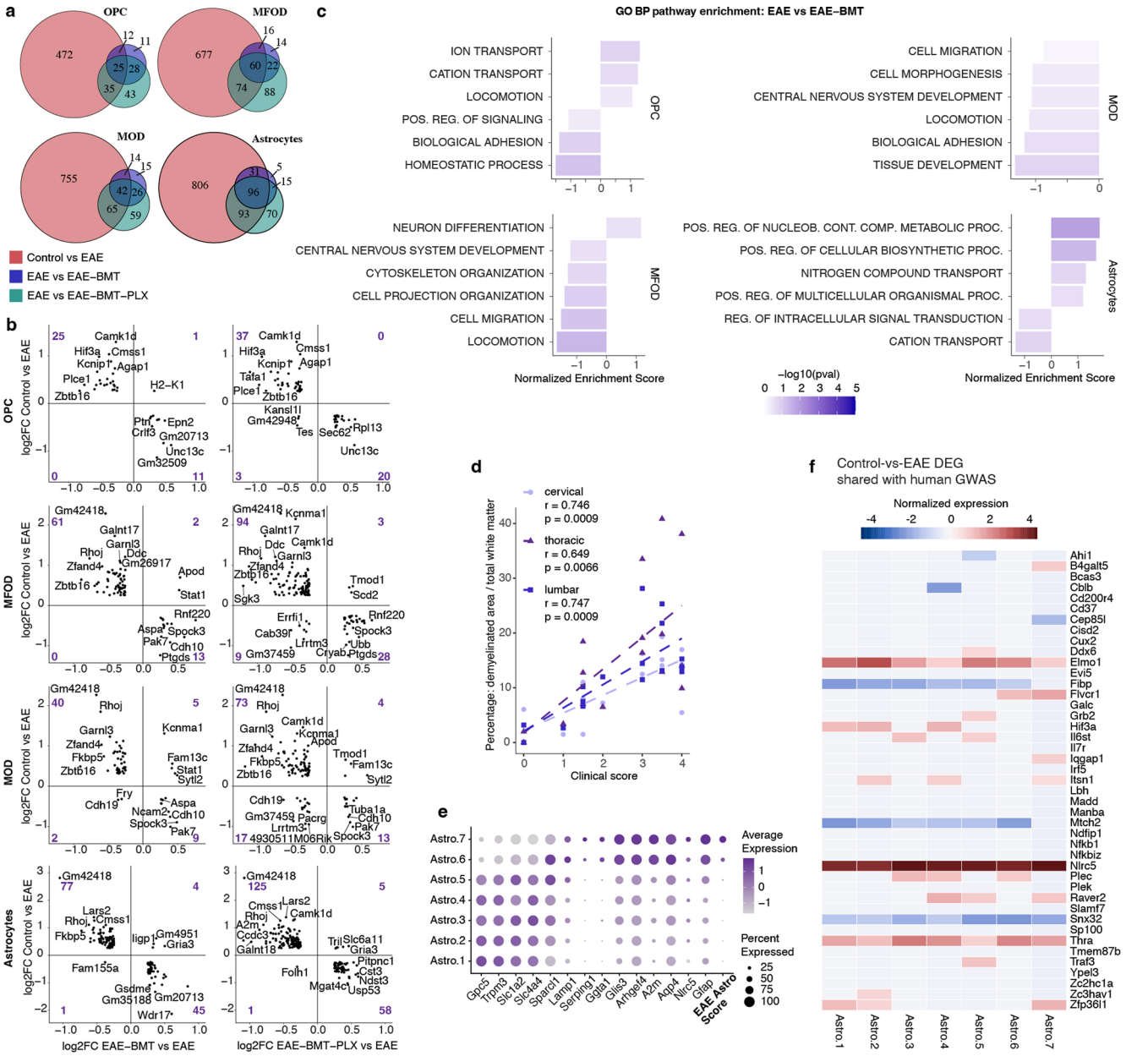
Extended Data Fig. 7 | Active MS brain lesions demonstrate myeloid cell expansion and activation. a, Relative distribution of main cluster groups between different original datasets and control/MS conditions. **b**, Relative proportion of the myeloid and lymphocyte cell clusters. Dots represent proportions per individual original sample (n = 54 total samples derived from brain and 6 from spinal cord). A/CA, active / chronic active lesion; CI, inactive lesion; WM, white matter. Two-sided Welch t-test. **c**, Number of significant DEGs (padj < 0.05, based on MAST) per main cell type between the *Control* and *MS* condition. Only cell types with significant DEGs are shown. **d**, Expression of the human orthologs of the cell type specific EAE Scores in the myeloid, oligodendrocyte, and astrocyte subclusters (p values based on two-sided Mann–Whitney U test with Holm method adjustment). **e**, UMAP plots of the subclusters of the immune cells of the human brain (left panel, 7822 nuclei) and spinal cord (right panel, 794 nuclei) datasets. **f**, Annotation and marker genes of brain (upper panel) and spinal cord (lower panel) immune subclusters. **g**, Distribution of cell populations between *Control* and *MS* samples for the human brain (left panel) and spinal cord (right panel). Notably, the category 'Remyel' consists of only 2 nuclei. **h**, Expression of the human ortholog of the EAE Myeloid Score in myeloid subclusters of the human brain (upper panel) and spinal cord (lower panel) datasets. **i**, Expression of IQGAP1 in the brain myeloid cluster. Box plot elements represent median (center line), first and third quartiles (lower and upper hinges) and smallest/highest value with at most 1.5*IQR (inter-quartile range) from the hinge (whiskers).

https://doi.org/10.1038/s41593-024-01609-3



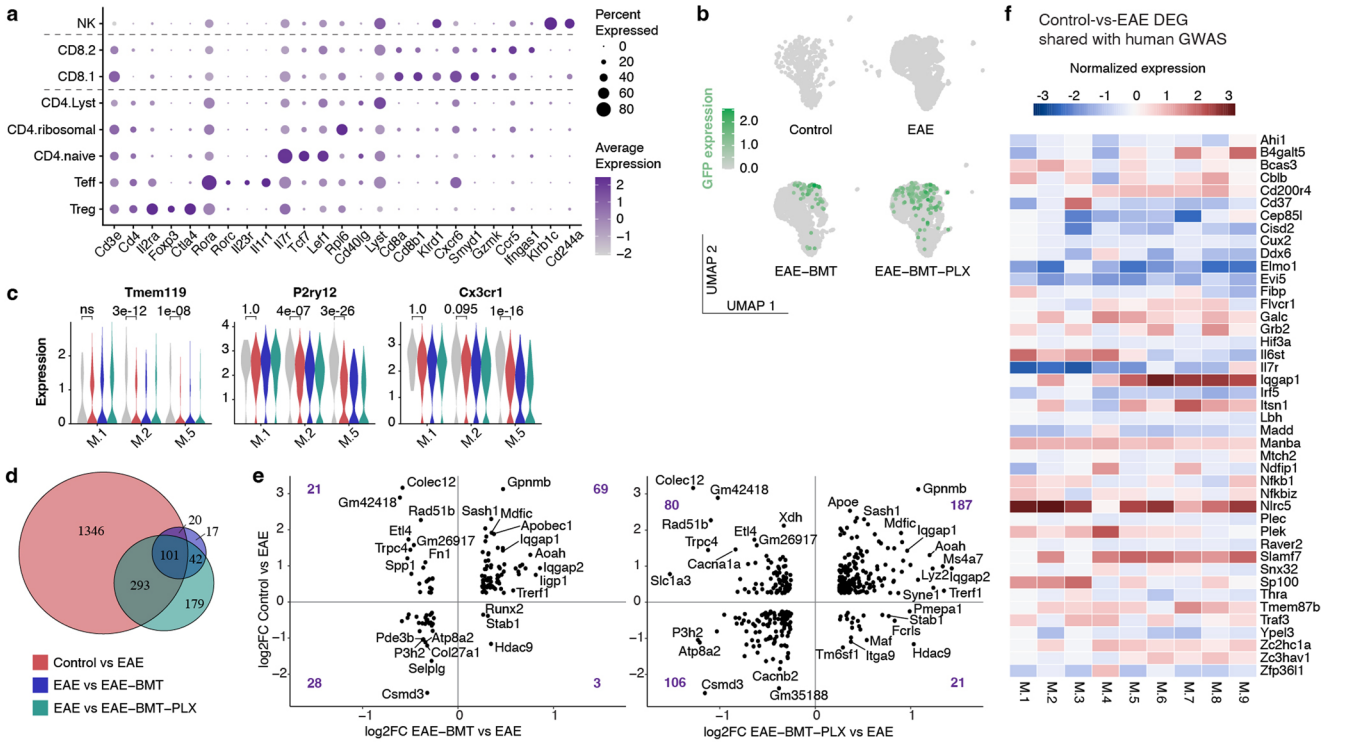
Extended Data Fig. 8 | BMT-induced morphological changes in myeloid cells are present in both spinal cord and brain. a, Representative FACS gating strategy to quantify GFP chimerism in peripheral blood. **b**, Representative images of GFP+ chimerism in brain myeloid cells. Scale bars are 100 µm. **c**, Quantification of GFP positive and negative Iba1+ cells. Dots represent the average of multiple measurements per animal. A total of 17 animals or 26 animals were analyzed for spinal cord or brain regions, respectively. **d**, Pearson correlation coefficient (r) and scatter plot demonstrate the correlation between brain and spinal cord GFP+ chimerism. Regression line based on linear model. Two-sided test. **e**, A gene signature for CDMCs was based on previously published 1296 DEGs between CDMCs and endogenous microglia[25] and a score was calculated with the VISION pipeline. Expression in the myeloid cluster is demonstrated. **f**, The fractions of nuclei in the myeloid cluster with a CDMC score expression of >−0.05 are shown (total n = 8 sequencing libraries derived from 14 spinal cords). **g**, Quantification of maximum branch length of ramified myeloid cells of the spinal cord in different conditions. Each dot represents one cell (total n = 210), dot colors represent different animals (n = 12). Two-sided Mann–Whitney U test. **h**, Representative immunofluorescent images of ramified myeloid cells in the brain. Brightness/contrast was adjusted individually per image for morphological assessment due to differing Iba1 intensity between conditions. Scale bars are 20 µm. **i**, Morphological analysis of ramified myeloid cells of the cortex in different conditions. Each dot represents one cell (total n = 162), dot colors represent different animals (n = 15). Two-sided Mann–Whitney U test. Box plot elements represent median (center line), first and third quartiles (lower and upper hinges) and smallest/highest value with at most 1.5*IQR (inter-quartile range) from the hinge (whiskers).

https://doi.org/10.1038/s41593-024-01609-3



Extended Data Fig. 9 | Transcriptional changes in astrocytes and oligodendrocytes in the context of EAE and BMT. a, Venn diagrams of DEGs (padj < 0.05, based on MAST with Bonferroni correction) between selected conditions for main oligodendrocyte and astrocyte clusters. **b**, Scatterplots show the relationship of significant DEGs (padj < 0.05 for both conditions, based on MAST with Bonferroni correction) of disease-associated (*Control vs EAE*) and treatment-associated (*EAE vs EAE-BMT* or *EAE vs EAE-BMT-PLX*) conditions of different oligodendrocyte and astrocyte clusters. Purple numbers represent the DEGs per quadrant. **c**, Gene set enrichment analysis based on differentially expressed genes between the *EAE* and *EAE-BMT* groups in selected clusters. Shown are the top six Gene Ontology (GO) Biological Process (BP) pathways based on GSEA-derived p values. Terms are abbreviated to fit the format. A complete list can be found in Supplementary Table 3. **d**, Correlation between white matter demyelination and clinical score. Regression lines based on linear models; r = Pearson correlation coefficient. Two-sided test. **e**, Expression of marker genes and EAE Astro Score in astrocyte subclusters. **f**, Expression profile of DEGs shared with genes of a multiple sclerosis genome wide association study (GWAS) for astrocyte subclusters. Expression values (average log2 fold-change) are normalized by columns. If no significant DEG was present for a cell type, the value 0 was applied.

https://doi.org/10.1038/s41593-024-01609-3



Extended Data Fig. 10 | Transcriptional changes in myeloid cells in the context of EAE and BMT. a, Marker gene expression of different T cell populations. NK, natural killer cells. Teff, effector T cells. Treg, regulatory T cells. **b**, Expression of GFP in nuclei of the myeloid cluster. Ordered towards the front based on expression. **c**, Expression of selected microglia marker genes in clusters M.1, M.2, and M.5 in different conditions. Adjusted p values based on DEG analysis (MAST with Bonferroni correction), compare also Supplementary Table 16. **d**, Venn diagram showing significant DEGs (padj <0.05, based on MAST with Bonferroni correction) of the myeloid cluster between different conditions. **e**, Scatterplots show the relationship of significant DEGs (padj < 0.05 for both conditions, MAST with Bonferroni correction) of disease-associated (*Control vs EAE*) and treatment-associated (*EAE vs EAE-BMT* or *EAE vs EAE-BMT-PLX*) conditions of the myeloid cluster. Purple numbers represent the DEGs per quadrant. **f**, Expression profile of DEGs shared with genes of a multiple sclerosis genome wide association study (GWAS) for myeloid subclusters. Expression values (average log2 fold-change) are normalized by columns. If no significant DEG was present for a cell type, the value 0 was applied.

nature portfolio

Corresponding author(s): Marius Wernig

Last updated by author(s): Jan 2, 2024

Reporting Summary

Nature Portfolio wishes to improve the reproducibility of the work that we publish. This form provides structure for consistency and transparency in reporting. For further information on Nature Portfolio policies, see our Editorial Policies and the Editorial Policy Checklist.

Statistics

For all statistical analyses, confirm that the following items are present in the figure legend, table legend, main text, or Methods section.

n/a	Confirmed
☐	☒ The exact sample size (*n*) for each experimental group/condition, given as a discrete number and unit of measurement
☐	☒ A statement on whether measurements were taken from distinct samples or whether the same sample was measured repeatedly
☐	☒ The statistical test(s) used AND whether they are one- or two-sided *Only common tests should be described solely by name; describe more complex techniques in the Methods section.*
☒	☐ A description of all covariates tested
☐	☒ A description of any assumptions or corrections, such as tests of normality and adjustment for multiple comparisons
☐	☒ A full description of the statistical parameters including central tendency (e.g. means) or other basic estimates (e.g. regression coefficient) AND variation (e.g. standard deviation) or associated estimates of uncertainty (e.g. confidence intervals)
☐	☒ For null hypothesis testing, the test statistic (e.g. *F*, *t*, *r*) with confidence intervals, effect sizes, degrees of freedom and *P* value noted *Give P values as exact values whenever suitable.*
☒	☐ For Bayesian analysis, information on the choice of priors and Markov chain Monte Carlo settings
☒	☐ For hierarchical and complex designs, identification of the appropriate level for tests and full reporting of outcomes
☐	☒ Estimates of effect sizes (e.g. Cohen's *d*, Pearson's *r*), indicating how they were calculated

Our web collection on statistics for biologists contains articles on many of the points above.

Software and code

Policy information about availability of computer code

Data collection	For Droplet-based single nuclei RNA sequencing: Main cohort: Illumina sequencing of the libraries was performed by Novogene (https://en.novogene.com/) on an Illumina NovaSeq S4 (Illumina). Base calling, demultiplexing, and generation of FastQ files were conducted by Novogene. Control cohort: Illumina sequencing of the libraries was performed on an Illumina NextSeq 550 (Illumina). Base calling, demultiplexing, and generation of FastQ files for the control cohort data was conducted using the mkfastq command of the Cell Ranger software (v.6.1.2). The Cell Ranger (v.6.1.2) analysis pipelines were utilized to align reads to the mm10 reference genome as well as GFP, and count barcodes/UMIs. For the control cohort, cell demultiplexing by assigning hashtag antibody oligo tags to cell-associated barcodes was performed with the Cell Ranger multi pipeline. For, the human spinal cord dataset from Trobisch et al., the Cell Ranger (v.6.1.2) analysis pipelines were utilized to align reads to the GRCh38 reference genome. Flow cytometry: FACSDiva software (BD Biosciences) and Sony MA900 Multi-Application Cell Sorter software Microscopy: ZEN blue (Zeiss, version 3.7.97.04000), Zen black (Zeiss, version 14.0.28.201), Leica Application Suite X (LAS X, Leica, versions 3.7.4.23463 and 3.5.7.23225)
Data analysis	R version 4.1.2 and 4.2.0 RStudio 2022.02.2+485 and 2022.02.3+492

R packages: seurat 4.2.0, fgsea 1.24.0, ggplot2 3.4.0, ggpubr 0.5.0, UpSetR 1.4.0, VennDiagram 1.7.3, ggrepel 0.9.2, shiny 0.61.1, sctransform 0.3.5, MAST 1.20.0, VISION 3.0.0, dplyr 1.10.0, tidyr 1.2.1, biomaRt 2.50.3

Fiji ImageJ 1.53q

FlowJo 10.8.1

For manuscripts utilizing custom algorithms or software that are central to the research but not yet described in published literature, software must be made available to editors and reviewers. We strongly encourage code deposition in a community repository (e.g. GitHub). See the Nature Portfolio guidelines for submitting code & software for further information.

Data

Policy information about availability of data

All manuscripts must include a data availability statement. This statement should provide the following information, where applicable:

- Accession codes, unique identifiers, or web links for publicly available datasets
- A description of any restrictions on data availability
- For clinical datasets or third party data, please ensure that the statement adheres to our policy

The murine sequencing datasets generated and analyzed in the current study are available in the Gene Expression Omnibus repository under accession numbers GSE217529 and GSE242512.

The human spinal cord dataset from Trobisch et al. was accessed as 6 fastq files (3 control and 3 MS patients) via Sequence Read Archive (SRA; accession number PRJNA726991).

Human brain NucSeq datasets were obtained as expression matrices from the UCSC Cell Browser (https://cells.ucsc.edu)73 and were originally generated by Absinta et al. (3 control and 5 MS patients [Cell Browser dataset ID: chronic-ms]), Jäkel et al. (5 control and 4 MS patients [Cell Browser dataset ID: oligodendrocyte-ms]), and Schirmer et al. (9 control and 12 MS patients [Cell Browser dataset ID: ms]).

Reference genomes (refdata-gex-mm10-2020-A and refdata-gex-GRCh38-2020-A) were accessed via www.10xgenomics.com.

Human research participants

Policy information about studies involving human research participants and Sex and Gender in Research.

Reporting on sex and gender	N/A
Population characteristics	N/A
Recruitment	N/A
Ethics oversight	N/A

Note that full information on the approval of the study protocol must also be provided in the manuscript.

Field-specific reporting

Please select the one below that is the best fit for your research. If you are not sure, read the appropriate sections before making your selection.

☒ Life sciences ☐ Behavioural & social sciences ☐ Ecological, evolutionary & environmental sciences

For a reference copy of the document with all sections, see nature.com/documents/nr-reporting-summary-flat.pdf

Life sciences study design

All studies must disclose on these points even when the disclosure is negative.

Sample size	No specific sample size calculation was performed due to the pilot character of the study exploring the only scarcely studied chronic stage of EAE and unknown effect sizes of hematopoietic cell transplantations in this model. However, previous publications on EAE in general were considered for choosing the sample sizes applied in this study.
Data exclusions	Sequencing data: Exclusion of nuclei that were deemed of low quality (debris) or suspected doublets. Specifically, for the murine dataset, Seurat objects were generated including features expressed by at least a minimum of 3 cells and including cells with expression of at least 50 features. Outliers with a ratio of mitochondrial relative to endogenous RNAs of >5%, homotypic doublets (>6,000 features in main and >4,000 features in control cohort) and debris (<400 features in main and <500 features in control cohort) were removed. After each integration, clustering, and subclustering step, clusters / subclusters were manually inspected for gene expression profiles and cell type-specific marker genes, and suspected doublets and debris were removed for downstream analysis. A small subcluster with Schwann cell signature was

removed in the T cell subcluster analysis.

EAE model: EAE animals without clinical presentation (clinical score = 0) were excluded from the experiments before the initiation of any therapeutic measures. Animals with mortality before day 50 were excluded from the analysis. One animal of the EAE-BMT-PLX group was sacrificed on day 76 due to non-EAE related reasons (with clinical score of 1.5) and was excluded from the analysis after this timepoint. Only animals surviving until the defined endpoints of the study were used for histological analysis.

For the human brain dataset of Schirmer et al., nuclei with a maximum number of 10,000 features were used and duplicated gene symbols were kept as distinct genes. No further adaptions were made to the other two human brain datasets before integration. For the human spinal cord dataset (generated by Trobisch et al.), Seurat objects were created per library, including features expressed by at least a minimum of 3 cells and including cells with expression of at least 50 features. Outliers with a ratio of mitochondrial relative to endogenous RNAs of >5% were removed. Thresholds for features were based on inspection of the separate objects and were as follows: SRR14408223: >150 & <1500; SRR14408224, SRR14408225, SRR14408231, SRR14408232: >300 & <3000; SRR14408226: >200 & <2000. After clustering and subclustering, the integrated human datasets were inspected and suspected doublet/debris cluster were removed as outlined above. Similarly, non-immune cell cluster were removed for the immune cell subcluster analysis.

Replication

Multiple biological replicates were used in this study, and clinical data was based on two independent cohorts. Specifically, the following total numbers of animals were used per experimental group:
Healthy controls: n = 8
CFA controls: n = 4
EAE (without intervention): n = 9
EAE with PLX: n = 4
EAE with BMT: n = 8
EAE with BMT+PLX: n = 9
All of these indicted EAE replicates demonstrated successful induction of the EAE phenotype as assessed with the EAE score. CFA control animals developed no EAE neurological phenotype but skin lesions. As detailed in the manuscript, we observed variability within the experimental groups. Therefore, we refer to the trends and significant effects between groups described in the manuscript for a detailed assessment of replication success.

Four independent, previously reported human datasets were analyzed.

Randomization

Animals were randomly assigned to experimental groups. Samples for downstream analysis were generated from these randomized animals.

Blinding

Investigators were blinded for clinical scoring (data collection), microscopy (data collection), and quantification of histological data (data analysis). No blinding was deemed feasible for the computational analysis of sequencing data due to the exploratory character of this analysis.

Reporting for specific materials, systems and methods

We require information from authors about some types of materials, experimental systems and methods used in many studies. Here, indicate whether each material, system or method listed is relevant to your study. If you are not sure if a list item applies to your research, read the appropriate section before selecting a response.

Materials & experimental systems

n/a	Involved in the study
☐	☒ Antibodies
☒	☐ Eukaryotic cell lines
☒	☐ Palaeontology and archaeology
☐	☒ Animals and other organisms
☒	☐ Clinical data
☒	☐ Dual use research of concern

Methods

n/a	Involved in the study
☒	☐ ChIP-seq
☐	☒ Flow cytometry
☒	☐ MRI-based neuroimaging

Antibodies

Antibodies used

Primary antibodies for immunofluorescence staining:
C4 abcam ab11863 rat 1:100
CD206 R&D systems AF2535 goat 1:40
GFAP Invitrogen 13-0300 rat 1:500
GFP abcam ab13970 chicken 1:1000
Iba1 FUJIFILM Wako 019-19741 rabbit 1:1000
Iba1 abcam ab5076 goat 1:500
IQGAP1 abcam ab133490 rabbit 1:50 or 1:100
Olig2 Millipore Sigma AB9610 rabbit 1:1000 (polyclonal)
Spp1 Santa Cruz Biotechnology sc-21742 mouse 1:40
Stat1 Cell Signaling 14994 rabbit 1:200
Galectin3 Biolegend 125401 rat 1:100
NLRC5 abcam ab105411 rabbit 1:200

For flow cytometry:

NeuN Abcam ab190565 AlexaFluor647 1:200
Olig2 Sigma MABN50A4 AlexaFluor488 1:100 (clone 211F1.1)
CD45 Biolegend 103112 APC 1:200
CD11b Invitrogen 12-0112-82 PE 1:200

For cell hashing:
Anti-Nuclear Pore Complex Protein Hashtag antibodies (TotalSeq™-A0451, -A0452, -A0453, and -A0455, Biolegend, 682205, 682207, 682209, and 682213)

Validation

C4 abcam ab11863
https://www.abcam.com/products/primary-antibodies/c4-antibody-16d2-ab11863.html
Suitable for: IHC-Fr; Reacts with: Mouse

CD206 R&D systems AF2535
https://www.rndsystems.com/products/mouse-mmr-cd206-antibody_af2535
Species Reactivity Mouse
Immunohistochemistry: MMR/CD206 was detected in perfusion fixed frozen sections of mouse lung using Goat Anti-Mouse MMR/CD206 Antigen Affinity-purified Polyclonal Antibody (Catalog # AF2535) at 25 µg/mL overnight at 4 °C.

GFAP Invitrogen 13-0300
https://www.thermofisher.com/antibody/product/GFAP-Antibody-clone-2-2B10-Monoclonal/13-0300
Applications Immunohistochemistry (IHC)
Tested Dilution 10-50 µg/mL
Species Reactivity Bovine, Human, Mouse, Rat
Published species Ferret, Guinea pig, Human, Mouse, Pig, Rat

GFP abcam ab13970
https://www.abcam.com/products/primary-antibodies/gfp-antibody-ab13970.html
Suitable for: WB, ICC/IF
Reacts with: Species independent

Iba1 FUJIFILM Wako 019-19741
https://labchem-wako.fujifilm.com/us/product/detail/W01W0101-1974.html
Reactivity : mouse, rat
Applications Immunohistochemistry (Frozen Section) 1:500 - 1,000

Iba1 abcam ab5076
https://jneuroinflammation.biomedcentral.com/articles/10.1186/s12974-022-02651-3#Sec2
PMID: 36463233 DOI: 10.1186/s12974-022-02651-3

IQGAP1 abcam ab133490
https://www.abcam.com/products/primary-antibodies/iqgap1-antibody-epr5220-ab133490.html
Suitable for: Flow Cyt (Intra), WB, IHC-P, ICC/IF
Knockout validated
Reacts with: Mouse, Human

Olig2 Millipore Sigma AB9610 rabbit 1:1000 (polyclonal)
https://www.emdmillipore.com/US/en/product/Anti-Olig-2-Antibody,MM_NF-AB9610
Species Reactivity Note: Human, rat and mouse. Other species have not been tested.
Application: Anti-Olig-2 Antibody is an antibody against Oligodendrocyte transcription factor 2 for use in IC, IH, IH(P), IP and WB.

Spp1 Santa Cruz Biotechnology sc-21742
https://www.scbt.com/p/opn-antibody-akm2a1
Applications: WB, IP, IF, IHC(P)
Species Reactivity/Detection: mouse, rat, human

Stat1 Cell Signaling 14994
https://www.cellsignal.com/products/primary-antibodies/stat1-d1k9y-rabbit-mab/14994
Specificity / Sensitivity: Stat1 (D1K9Y) Rabbit mAb recognizes endogenous levels of total Stat1 protein. This antibody also cross-reacts with an unidentified protein of 150 kDa.
Species Reactivity: Human, Mouse, Rat, Monkey
Application Immunofluorescence (Immunocytochemistry) Dilution 1:200 - 1:800
See also PMID: 29018057

Galectin3 Biolegend 125401
https://www.biolegend.com/en-ie/products/purified-anti-mouse-human-mac-2-galectin-3-antibody-4935
Verified Reactivity: Mouse, Human
Application: ICC, WB, IP - Verified

NLRC5 abcam ab105411
https://www.abcam.com/products/primary-antibodies/nlrc5-antibody-ab105411.html
Reacts with: Mouse
Application for Immunofluorescence see reference:
https://onlinelibrary.wiley.com/doi/10.1111/jnc.14876
PMID: 31549732 DOI: 10.1111/jnc.14876

NeuN Abcam ab190565 AlexaFluor647
https://www.abcam.com/products/primary-antibodies/alexa-fluor-647-neun-antibody-epr12763-neuronal-marker-ab190565.html
Suitable for: IHC-P, ICC/IF, IHC-Fr
Reacts with: Mouse, Rat, Human

Olig2 Sigma MABN50A4 AlexaFluor488
https://www.emdmillipore.com/US/en/product/Anti-Olig2-Antibody-clone-211F1.1-Alexa-Fluor488-Conjugate-MABN50A4,MM_NF-MABN50A4
Species Reactivity Note: Demonstrated to react with mouse and rat.
IC staining of undifferentiated rat OPCs using a 1:100 dilution of Anti Olig2 (MABN50) and counterstained with DAPI. Staining of this transcription factor is shown primarily nuclear.

CD45 Biolegend 103112 APC
https://punchout.biolegend.com/en-us/products/apc-anti-mouse-cd45-antibody-97
Verified Reactivity Mouse
Application FC - Quality tested

CD11b Invitrogen 12-0112-82 PE
https://www.thermofisher.com/antibody/product/CD11b-Antibody-clone-M1-70-Monoclonal/12-0112-82
Applications Flow Cytometry (Flow) Tested Dilution 0.125 µg/test
Species Reactivity Mouse
Published species Dog, Fish, Human, Mouse

Animals and other research organisms

Policy information about studies involving animals; ARRIVE guidelines recommended for reporting animal research, and Sex and Gender in Research

Laboratory animals	Female C57BL/6J mice were used for the EAE model (JAX, Strain 000664). The C57BL/6-Tg(UBC-GFP)30Scha/J strain (JAX, Strain 004353) was crossed with wild-type C57BL/6J mice to generate hemizygote UBC-GFP animals. Female hemizygote UBC-GFP mice of 10-12 weeks were used as donor animals for BMT. EAE was induced in female C57BL/6J mice at the age of 11 weeks.
Wild animals	The study did not involve wild animals
Reporting on sex	Only female animals were used according to the instructions of the EAE induction kit (Hooke Laboratories)
Field-collected samples	The study did not involve field-collected samples
Ethics oversight	All animal procedures were approved by the administrative panel on laboratory animal care at Stanford University (APLAC21565).

Note that full information on the approval of the study protocol must also be provided in the manuscript.

Flow Cytometry

Plots

Confirm that:

☒ The axis labels state the marker and fluorochrome used (e.g. CD4-FITC).

☒ The axis scales are clearly visible. Include numbers along axes only for bottom left plot of group (a 'group' is an analysis of identical markers).

☒ All plots are contour plots with outliers or pseudocolor plots.

☒ A numerical value for number of cells or percentage (with statistics) is provided.

Methodology

Sample preparation

Tissue collection for the transcriptomic analysis was performed 3 months after EAE induction or in an age-matched healthy control animal. Animals were anesthetized (100 mg/kg of ketamin and 10 mg/ kg of xylazine, i.p.) and transcardially perfused. Spinal cords were harvested by hydraulic expulsion and snap-frozen by submerging for 60 seconds in liquid nitrogen-cooled isopentane. Frozen spinal cords were stored at -80°C until further processing. Single-nuclei preparation was performed as previously described with the following modifications.63 The thoracolumbar section of spinal cords were first mechanically dissociated with an ice-cold razor blade in a petri dish with 1ml EZ Prep lysis buffer (Sigma, NUC-101) on ice. Transfer of tissue suspension into a 2ml glass dounce tissue grinder tube (Sigma, D8938). Petri dish was rinsed off with another 1ml EZ buffer, which was added to the grinder tube. Suspension was homogenized by hand 25 times with pestle A followed by 25 times with pestle B while incorporating a 180-degree twist. Tissue homogenate was transferred to a fresh 15ml tube on ice. The grinder tube was rinsed with 2 ml fresh lysis buffer, which was added to the 15ml tube for a total volume of 4 ml. Samples were incubated on ice for 5 minutes. Nuclei were centrifuged at 500 x g for 5 minutes at 4°C, supernatant was removed, and the pellet resuspended with 4 ml EZ lysis buffer and incubated on ice for 5 minutes. Centrifugation at 500 x g for 5 minutes at 4°C was repeated. After removing the supernatant, the pellet was resuspended with 4 ml chilled PBS and filtered through a 35-um cell strainer into a 5 ml round bottom FACS tube (Corning, 352235). Following centrifugation at 300

x g for 10 minutes at 4°C with break 3, supernatant was gently poured out leaving behind the nuclei pellet. The pellet was resuspended in 100µl FC block buffer (BD Biosciences, 553141, 1:50 in FACS buffer) and 1ul recombinant RNase inhibitor (Takara, 2313B) incubated on ice for 5min. FACS buffer consisted of PBS (Gibco, 10010049) containing 1% BSA (Thermo Fisher, BP9700100)). To 50µl of the cell suspension, we added 150µl FACS buffer with 2µl Olig2-Alexa Fluor488 (Sigma, MABN50A4), 1ul NeuN-AlexaFluor647 (Abcam, ab190565), and 1.5ul RNase inhibitor. Anti-Nuclear Pore Complex Protein Hashtag antibodies (1 µl) were additionally added to the samples of the control cohort (TotalSeq™-A0451, -A0452, -A0453, and -A0455, Biolegend, 682205, 682207, 682209, and 682213). After 30min incubation covered from light and shaking on ice, 3ml FACS buffer were added. Following centrifugation at 300 x g for 10 minutes at 4°C with break 3, supernatant was gently poured out. The pellet was resuspended in 700µl FACS buffer with 3.5ul recombinant RNase inhibitor and Hoechst dye (Thermo Fisher, H3570, 1:2000) and incubated 4min on ice covered from light. Single nuclei were sorted on a MA900 Multi-Application Cell Sorter (Sony Biotechnology) gating for NeuN negative nuclei.

Peripheral blood was collected from the facial vein and treated with 0.5M EDTA. Erythrocytes were removed by 10 minutes of incubation in 2ml ice-cold RBC lysis buffer.62 Cells were collected via centrifugation for 10min at 300g. Cells were washed with PBS and then stained for 15min at 4 °C in Flow buffer (PBS with 5% cosmic calf serum) containing the following antibodies: CD11b-PE (Invitrogen, 12-0112-82), CD45-APC (Biolegend, 103112). Stained cells were washed in PBS and resuspended in Flow buffer with DAPI (Sigma, D9542).

Instrument

FACS AriaII for peripheral blood analysis
MA900 Multi-Application Cell Sorter (Sony Biotechnology) for nuclei sorting

Software

Data collection: FACSDiva software (BD Biosciences) and Sony MA900 Multi-Application Cell Sorter software
Analysis: FlowJo 10.8.1

Cell population abundance

Nuclei were counted using a hemacytometer (Sigma, Z359629-1EA) and assessed for concentration and quality.

Gating strategy

Peripheral blood analysis: single cell gates (SSC-A/FSC-A -> FSC-H/FSC-A) -> live cell gate (DAPI negative) -> APC-CD45+ PE-CD11b+ gate -> GFP+ gate
Nuclei sorting: single nuclei (BSC-A/FSC-A -> Hoechst+) -> AlexaFluor647-NeuN- FITC-Olig2+

☒ Tick this box to confirm that a figure exemplifying the gating strategy is provided in the Supplementary Information.